Journal of the Atmospheric Sciences

A Study on the Asymmetric Rapid Intensification of Hurricane Earl (2010) using the HWRF System

--Manuscript Draft--

Manuscript Number:	JAS-D-14-0097
Full Title:	A Study on the Asymmetric Rapid Intensification of Hurricane Earl (2010) using the HWRF System
Article Type:	Article
Corresponding Author:	Sundararaman G. Gopalakrishnan, Ph.D AOML/NOAA Miami, FL UNITED STATES
Corresponding Author's Institution:	AOML/NOAA
First Author:	Hua Chen
Order of Authors:	Hua Chen
	Sundararaman G. Gopalakrishnan, Ph.D
Abstract:	In this study, the results of a forecast from the operational Hurricane Weather Research and Forecasting (HWRF) system for Hurricane Earl (2010) are verified against available observations and analyzed to understand the asymmetric rapid intensification of a storm in a sheared environment. The forecast verification shows that the HWRF model captured well Earl's observed evolution of intensity, convection asymmetry, wind field asymmetry, and vortex tilt in terms of both magnitude and direction in the pre-rapid and rapid intensification (RI) stages. Examination of the high-resolution forecast data reveals that the tilt was large at the RI onset and decreased quickly once RI commenced, suggesting that vertical alignment is the result instead of the trigger for RI. The RI onset is associated with the development of upper-level warming in the eye center, which results from upper-level storm-relative flow advecting the subsidence warming in the upshear-left region towards the low-level storm center. This scenario does not occur until persistent convective bursts (CBs) are concentrated in the downshear-left quadrant. The temperature budget calculation indicates that horizontal advection plays an important role in the development of upper-level warming in the early RI stage. The upper-level warming associated with the asymmetric intensification process occurs by means of the cooperative interaction of the convective-scale subsidence, resulting from CBs in favored regions and the shear-induced mesoscale subsidence. When CBs are concentrated in the downshear-left and upshear-left quadrants, the subsidence warming is maximized upshear and then advected towards the low-level storm center by the storm-relative flow at the upper level. Subsequently, the surface pressure falls and RI occurs.

Copyright Form

Click here to download Copyright Form: CopyRight.pdf

Cost Estimation and Agreement Worksheet

Click here to download Cost Estimation and Agreement Worksheet: Cost Estimation and Agreement Worksheet.pdf

Response to Editor

Ref.: JAS-D-14-0097
Journal of the Atmospheric Sciences
Editor Decision

Prof. Ka-Kit Tung: Thanks for your e-mail message ushering us on the size of our manuscript. We are submitting a substantially downsized version of the manuscript. FYI: Although there have been several research publications on the NOAA HWRF system, at the time of writing this publication, there was not a single documented effort that described the end to end operational system (hurricane physics, initialization). Part of the size problem may be attributed to that. That section may not impact the scientific content of our work, nevertheless, we thought the information was essential for the reviewer as well as the readers. Nevertheless, we appreciate your concerns, as well. We have now taken great care to reduce that (technical) section substantially, yet citing several related references. Those reductions plus a few other edits have brought down the size of the manuscript to about 8200 words (excluding the abstract, references, citations and acknowledgements). We will be more than happy to furnish the technical details of the model if the reviewers wish to see those. Unfortunately, anything below this margin is starting to affect the scientific contents of this work. Hope you may be able to consider the revised version for further processing now.

Regards
Gopal

Sundararaman.G.Gopalakrishnan, Ph.D
Modeling Team Leader & Sr.Meteorologist
Hurricane Research Division/AOML/NOAA
4301 Rickenbacker Causeway, Miami, FL
Phone: 305-361-4357
http://hwrf.aoml.noaa.gov/

A Study on the Asymmetric Rapid Intensification of Hurricane Earl (2010) using the HWRF System

Hua Chen

Rosenstiel School of Marine and Atmospheric Science, University of Miami, and
NOAA/AOML/Hurricane Research Division, Miami, Florida

Sundararaman G. Gopalakrishnan

NOAA/Atlantic Oceanographic and Meteorological Laboratory/Hurricane Research Division,
Miami, Florida

Submitted to *Journal of the Atmospheric Sciences*

25 April 2014

Corresponding author:
Dr.Sundararaman G. Gopalakrishnan
NOAA/AOML/ Hurricane Research Division
4301 Rickenbacker Causeway, Miami, FL 33149
Tel. (305) 361-4357
Fax: (301) 361-4402
Email: gopal@noaa.gov

Abstract

In this study, the results of a forecast from the operational Hurricane Weather Research and Forecasting (HWRF) system for Hurricane Earl (2010) are verified against available observations and analyzed to understand the asymmetric rapid intensification of a storm in a sheared environment. The forecast verification shows that the HWRF model captured well Earl's observed evolution of intensity, convection asymmetry, wind field asymmetry, and vortex tilt in terms of both magnitude and direction in the pre-rapid and rapid intensification (RI) stages. Examination of the high-resolution forecast data reveals that the tilt was large at the RI onset and decreased quickly once RI commenced, suggesting that vertical alignment is the result instead of the trigger for RI. The RI onset is associated with the development of upper-level warming in the eye center, which results from upper-level storm-relative flow advecting the subsidence warming in the upshear-left region towards the low-level storm center. This scenario does not occur until persistent convective bursts (CBs) are concentrated in the downshear-left quadrant. The temperature budget calculation indicates that horizontal advection plays an important role in the development of upper-level warming in the early RI stage. The upper-level warming associated with the asymmetric intensification process occurs by means of the cooperative interaction of the convective-scale subsidence, resulting from CBs in favored regions and the shear-induced mesoscale subsidence. When CBs are concentrated in the downshear-left and upshear-left quadrants, the subsidence warming is maximized upshear and then advected towards the low-level storm center by the storm-relative flow at the upper level. Subsequently, the surface pressure falls and RI occurs.

1. Introduction

Predicting the rapid intensification (RI) of tropical cyclones (TCs) is a complex, challenging, and important forecast problem. The factors that are known to influence intensity change vary on scales ranging from several hundreds of kilometers (e.g., environmental shear, dry air, and upper-ocean structure) to a few kilometers (e.g., convective-scale asymmetries) and, sometimes, even down to a few hundred meters (e.g., wind gusts and aerosols). Although there is currently much less skill in forecasting RI with fidelity (Cangialosi and Franklin 2012), cloud-resolving numerical models using a horizontal grid resolution of 1–3 km have demonstrated the capability to capture the relevant processes. For instance, several recent studies have shown that vortical thermal plumes and the subsequent development of the warm core is one possible pathway for RI of at least an initially symmetric vortex (e,g., Hendricks et al. 2004; Montgomery et al. 2006; Nguyen et al. 2008; Gopalakrishnan et al. 2011; Chen and Zhang 2013). Indeed, recent observational studies (Harnos and Nesbitt 2011; Jiang 2012; Kieper and Jiang 2012; Rogers et al. 2013) also support the fact that the majority of RI cases are characterized by a symmetric ring of precipitation prior to RI onset. However, in the presence of vertical wind shear (VWS), which typically occurs in the tropical atmosphere, storms have also been observed to rapidly intensify (Molinari et al. 2006; Molinari and Vollaro 2010). Yet, such RI cases have received little attention. This may be due to the lack of routine high-resolution observations in space and time needed to support both the analysis of the convective-scale and mesoscale dynamical processes within storm core regions and verification of the model-based simulations.

In this study, we analyze the dynamic processes associated with RI under the influence of VWS for the case of Hurricane Earl (2010). The study capitalizes on the availability of a multi-day sequence of high-resolution observations collected during the National Oceanic and

Atmospheric Administration's (NOAA) hurricane field program campaign (Rogers et al. 2012; Montgomery et al. 2013) and the high-resolution forecast from the Hurricane Weather Research and Forecasting (HWRF) system that verified well in terms of track and intensity, as well as storm structure evolution, against available observations. The high skill of the forecast provides the basis for confidence in the forecast model representation of the relevant processes analyzed in this study.

Prior studies on the intensification of TCs have indicated that the development and enhancement of the warm core is a necessary condition for intensification. In a series of idealized HWRF simulations in a shear-free environment, Gopalakrishnan et al. (2011) showed that rapid warming of the core was closely associated with the development of organized, moist, vortical thermal plumes around the eyewall region. This study related warm core formation to a wind induced surface heat exchange type of feedback (Emanuel 1987) in the hurricane boundary layer wherein the surface pressure decreased (by hydrostatic principles), resulting in an increase in wind speed, surface enthalpy fluxes (θ_e) and, subsequently, a warmer core. In a study of Hurricane Wilma (Chen et al. 2011; Zhang and Chen 2012; Chen and Zhang 2013), the authors showed that an upper-level (i.e., z = 14 km) warm core formed, in coincidence with the RI onset, as a result of the descent of stratospheric air in the presence of weak, storm-relative flows aloft. The descent of stratospheric air resulted from the upper-level detrainment of convective bursts (CBs) occurring in the vicinity of the radius of maximum wind (RMW), where higher θ_e air was located. The associated subsidence warming did not become effective until an organized upper-level outflow was established with a weak cyclonic circulation and decreased static stability in the eye.

However, unlike the development of an axisymmetric vortex in an idealized, shear-free environment or the conducive large-scale environment in which Hurricane Wilma (2005) underwent an explosive intensification, a sheared environment (especially when the 850-200 hPa average shear is ≥ 5 m s^{-1}) is generally considered hostile to a developing TC and is likely to inhibit any rapid deepening mainly because of vortex tilt. Nevertheless, there are a few examples of TCs observed to have undergone RI in such a hostile environment. For instance, the surface pressure of Tropical Storm Gabrielle (2001) dropped 22 hPa in 3 h when the environmental deep layer shear was 13 m s^{-1}. Molinari et al. (2006) and Molinari and Vollaro (2010) reported some unprecedented findings from this case. These studies revealed that the RI of Gabrielle occurred when one intense convective cell that developed in the downshear left, where almost all radar return was located, moved cyclonically and inward to the 17-km radius, which was within the RMW and enhanced the efficiency for kinetic energy production. Another well documented case is Hurricane Guillermo (1997) (Eastin et al. 2005; Reasor et al. 2009; Sitkowski and Barnes 2009; Reasor and Eastin 2012). Eastin et al. (2005) used extensive airborne radar, dropwindsonde, and flight-level observations to illustrate typical azimuthal distribution of buoyant convection. They found that mesoscale vertical motions exhibited a wavenumber-1 structure with maximum ascent downshear and weak descent upshear with the downdraft core located upshear next to downshear deep convection. Reasor et al. (2009) demonstrated that the greatest intensification during the 6-h Doppler observation period coincided with the formation and cyclonic rotation of several particularly strong CBs through the left-of-shear semicircle of the eyewall when the deep layer shear was 7-8 m s^{-1}. The composite study of Corbosiero and Molinari (2002) used 35 Atlantic basin TCs from 1985–99 while they were over land and within 400 km of the coast over water. The authors discovered a strong correlation existed between the azimuthal distribution of lightning flashes and vertical wind shear in the environment, especially when the vertical wind shear exceeded 5 m s^{-1}.

Theoretical studies (Hack and Schubert 1986; Vigh and Schubert 2009) using the Eliassen-Sawyer equation have demonstrated that diabatic heating located inside the RMW is more efficient in intensifying the vortex. This conclusion was confirmed by a numerical study that explored the intensification of a balanced, baroclinic, tropical cyclone–like vortex in which convection was displaced from the vortex center (Nolan et al. 2007). The result from the Gabrielle case study (Molinari and Vollaro 2010) also confirmed this conclusion. In a composite of airborne Doppler data from multiple storms that were either intensifying or remaining steady-state, Rogers et al. (2013) showed that the radial location of the peak of the distribution of CBs was within the RMW for intensifying storms, whereas it was outside the RMW for steady-state storms. In an idealized study of the impact of shear on TC vortex intensification, Chen and Fang (2012) showed that weak shear induced downshear deep convection within the RMW because of small tilt and tended to facilitate TC intensification. In contrast, deep convection outside the RMW due to large vortex tilt in strong shear cases tended to curb TC intensification.

Other than the importance of the radial location of diabatic heating, a few studies have shown that the vortex tilt direction is also crucial for vortex intensification in a sheared environment. Using a dry adiabatic model, Reasor et al. (2004) demonstrated that TC-like vortices achieved approximate steady-state tilts to the left of the shear vector. In a real tropical environment, the vortex tilt may be more related to the location and timing of the deep convection. Indeed, in idealized experiments using a cloud-resolving model, Zhang and Tao (2013) showed that vortex tilt was determined by the location of deep convection in the presence of wavenumber-1 convection asymmetries. Both the vertical tilt of the vortex and the effective (local) vertical wind shear were considerably decreased after the tilt angle reached 90° to the left of the environmental shear. TCs intensified immediately after the 90° tilt and effective local shear reached their minima.

It should be noted that all of the above studies were either restricted to an observational analysis or dealt with a highly idealized environment which, at best, might provide insight on some aspect of the TC intensification process. The current work and associated publications are expected to bridge the gap between existing theoretical studies and observed findings specifically related to the rapid development of an initially asymmetric TC vortex in a sheared environment.

The next section describes the model configuration of the operational HWRF. Section 3 provides a brief overview of RI of Hurricane Earl. Section 4 presents verification of the model-predicted storm structures against various observations. Section 5 shows some model-predicted, inner-core structures and structural changes during Earl's pre-RI and RI stages. Section 6 demonstrates the formation of an upper-level warm core that is associated with the RI of Earl. Section 7 explains why RI occurs at that specific time. A summary and some concluding remarks are given in the final section.

2. The HWRF model, configuration, and physics

The triply-nested, cloud-resolving version of the operational HWRF system jointly developed by NOAA's National Weather Service/National Center for Environmental Prediction (NWS/NCEP) and the Hurricane Research Division (HRD) of the Atlantic Oceanographic and Meteorological Laboratory under the auspices of the Hurricane Forecast Improvement Project was used in this study (Gopalakrishnan et al. 2011, 2012, 2013; Tallapragada et al. 2013). In brief, this version has a number of important physics upgrades consisting of modifications to the NCEP Global Forecasting System (GFS) planetary boundary layer (PBL) based on observational findings (Gopalakrishnan et al. 2012; Zhang et al. 2013), improved Geophysical Fluid Dynamics Laboratory (GFDL) surface physics, improved Ferrier microphysics (Ferrier 1994), and implementation of the new GFS shallow convective parameterization (Hong and Pan 1996). HWRF's oceanic component is a version of the Princeton Ocean Model adapted for TCs (POM-TC; Yablonsky and Ginis 2008), which was developed at the University of Rhode Island. More details on the model parameterization schemes may be found in the above mentioned references.

HWRF uses a model-consistent vortex from the previous cycle that has been relocated and adjusted toward current pressure and wind observations (Liu et al. 2006; Tallapragada et al. 2013). This study uses output from the 1800 UTC 26 August 2010 retrospective forecast with vortex initialization and assimilation consisting of three major steps: (1) interpolation of the global analysis fields from the Global Forecast System (GFS) onto the operational 27:9:3 model grid; (2) removal of the GFS vortex from the global analysis; and (3) addition of the HWRF vortex modified from the previous cycle's 6-h forecast based on observed location and strength. The improved prediction of the HWRF system is partly attributed to the surface and boundary layer combination being reconstructed on the basis of hurricane observations and the advanced initialization procedure (Tallapragada et al. 2013; Goldenberg et al. 2014). For instance, forecast errors from the HWRF system for Earl were generally low, and those from the particular cycle used here were exceptional, as will be demonstrated in section 4. There were a few other cycles that could have been used; however, the current cycle captured the RI phase starting at 48 hours into the forecast so that any lack of realism related to initial conditions and subsequent spin up could be avoided.

3. Overview of RI of Hurricane Earl

A detailed account of Hurricane Earl is reported in Cangialosi (2010). In summary, the hurricane originated from a tropical easterly wave and organized into a tropical depression by 0600 UTC 25 August after acquiring sufficient convective organization when centered about 370 km west-southwest of the Cape Verde Islands. As convection became better organized, the system strengthened into a tropical storm by 1200 UTC 25 August and became a hurricane 1200 UTC 29 August in an environment with warm SSTs of 28-29ºC and moderate VWS. The hurricane underwent RI with a 21 m s^{-1} increase in wind speed over 24 h, becoming a category 4 hurricane by 1800 UTC 30 August as it slowed and gradually turned northwestward. In this work, we focus on the pre-RI and early RI forecasts (i.e., 1800 UTC 26 AUG to 1800 UTC 29 AUG).

4. Model verification

Figure 1 depicts the time evolution of Hurricane Earl in terms of central pressure, maximum 10-m wind, and the RMW[1]. Figure 1a shows the track of the storm from the HWRF forecast (red line) compared with the best track analysis (black line) plotted at a 6-h interval for the period of 1800 UTC 26 August to 1800 UTC 31 August. As can be seen, the predicted track follows the observations reasonably well, in general, and 95% of Earl's track errors are caused by the translation speed difference with the predicted hurricane moving slower than the observed hurricane. The track errors at 24 h, 48 h, and 72 h, critical for understanding the modeled intensification process, are 104 km, 177 km, and 181 km, respectively, and these numbers compare favorably to the season's best-track estimates of 104 km, 171 km, and 248 km for the same period (Cangialosi and Franklin 2011).

[1]It should be noted that the outputs from the model were plotted at higher frequency (i.e., 2 min) for further analysis. However, the observations are plotted at a 6-h interval and only provide a scale of measure of the model performance in terms of its overall behavior.

Figure 1b shows a time series of the central pressure from the HWRF (blue line) and best track analysis (black line), which indicates the HWRF forecast reproduced the central pressure change very well, particularly for the pre-RI and RI periods. Further examination of the pressure field shows there is a clear semidiurnal oscillation with 1.5 hPa amplitude. To obtain a clear signal that is related only to the storm itself, a filter with 1.5 hPa amplitude and 12-h period was applied to the time series of central pressure (blue line) and filtered time series of central pressure is depicted in red line. It captured the pre-RI stage, during which pressure remained almost unchanged in the first 27 h and deepened slightly between 27-51 h. The continuous steady deepening period began at 51 h. While the deepening rate between 51-57 h was only 0.1 hPa hr^{-1}, the deepening rate increased rapidly after 57 h, denoting RI onset for the HWRF forecast. Based on the maximum 10-m wind speed at 24 h, 48 h, and 72 h, the intensity errors were 0.8 m s^{-1}, 1 m s^{-1}, and 5 m s^{-1}, respectively, extremely good values when compared with the 2010 season intensity forecast errors of 6.5 m s^{-1}, 10.2 m s^{-1}, and 8.6 m s^{-1} (Cangialosi and Franklin 2011).

Figure 1c compares the time series of the RMW from the HWRF forecast and the observations. As can be seen, the RMW from the HWRF forecast is about 70 km smaller than the observations at the initial time, likely a result of cycling of the vortex from the previous run. It should be noted that while the vortex from the cycled runs was adjusted towards the observed central pressure, maximum 10-m wind speed, and radius of 17 m s^{-1} wind from the best track data, no initial adjustment for the RMW was performed in this initialization scheme. Nevertheless, after 24 h into the forecast, the RMW from HWRF is comparable to the observations, reaching about 110 km. Both the observed and simulated RMWs contract rapidly between 24-36 h. The contraction in the HWRF forecast with 2-min-resolution is realized through a series of significant fluctuations that may not be captured from the 6-h best track. As discussed later, these fluctuations are related to vigorous CBs that occur at different radii and quadrants. The RMW for both the observations and HWRF forecast remains nearly constant between 36-60 h with a slight contraction around 45 h. A large contraction in the RMW occurs after 60 h. The modeled RMW contracts from a radius of about 50 km to 20-30 km, consistent with the observations. The model verification in Fig.1 shows that the HWRF forecast reproduces the intensity and storm size exceptionally well for this cycle, making it an excellent case to provide further forecast insights on the intensification problem. Yet one question remains: Is this good forecast due to the right reasons? To answer this question, the forecasted environment and storm structure verifications will be examined first.

Figure 2 provides the mean large-scale environment from the HWRF forecast and GFS analysis in terms of VWS and SSTs. Although direct comparison of point value of shear and SSTs between low-resolution GFS analysis and a high-resolution ocean coupled HWRF system may be misleading, we use these comparisons to verify only the trend. As can be observed in Fig. 2a, both the HWRF shear (red line) and GFS shear (black line) show some oscillations around 5 m s^{-1}, and they are generally in phase with the amplitude of GFS shear about 2 m s^{-1} larger than that of HWRF shear. It is noteworthy that shear increases a few hours prior to RI and in the early RI stage for the HWRF forecast. As for the GFS analysis, shear also increases in the first 6 h of RI. Apparently, RI onset, at least in this case, is not caused by decreasing shear as postulated in earlier studies. Such studies suggested that shear curbs storm intensification through a number of pathways, including ventilation of the upper-level warm core (Frank and Ritchie 2001), middle-level ventilation that reduces the Carnot engine efficiency (Tang and Emanuel 2010), and reduced temperature in the boundary layer inflow (Riemer et al. 2010). Fig. 2b shows that SSTs increase drastically in the pre-RI stage in both the HWRF forecast and GFS analysis. As the storm approaches RI, the HWRF forecast SSTs almost level off, but the GFS SSTs continue increasing to 66 h. Nevertheless, the general trend is very similar, and the GFS SSTs are slightly warmer than the HWRF SSTs after RI onset. In this case, both the shear and SSTs imply that the role of environmental factors in controlling the RI of Earl is not clear-cut, providing a great example to study how multi-scale interaction leads to the RI of Earl.

Figure 3 compares radar reflectivity from the HWRF forecast at flight level (3-km altitude) against the lower fuselage radar observations available in the HRD database (http://www.aoml.noaa.gov/hrd/Storm_pages/earl2010/radar.html) for the pre-RI and RI stages. The snapshots from the HWRF forecast 1 h later and 2 h earlier are used in the pre-RI and RI stages, respectively, to verify the structure. In general, the convective asymmetry, which is governed by environmental shear, is also reproduced in the HWRF forecast. As can be seen, in the pre-RI stage when shear is northerly, the inner core is highly asymmetric with deep convection occurring roughly downshear and downshear-left in both the observed reflectivity and the HWRF forecast reflectivity. The magnitude of the northerly shear at this time is about 7.7 m s^{-1} and 5.3 m s^{-1}, respectively, for the observations and HWRF forecast. Most of the deep convection falls outside the 50-km radius for both the observations and HWRF forecast. After Earl begins RI, the shear remains northerly, and the reflectivity for both the observations and HWRF forecast is still highly asymmetric. Deep convection occurs downshear-left in the inner core and upshear in an outer rainband which is located at a larger radii in HWRF forecast than the observations. Although much of the high reflectivity due to convection falls outside the RMW for both the observations and the HWRF forecast, there is a significant amount of convection near the center (i.e., inside the 50-km radius), which is expected to increase the diabatic heating efficiency in intensifying the vortex as demonstrated in previous studies (Hack and Schubert 1986; Nolan et al. 2007; Vigh and Schubert 2009; Rogers et al. 2013).

Other than the wavenumber-1 asymmetry in the horizontal distribution of reflectivity, another major response of the storm structure to shear is vortex tilt with altitude. Figure 4 compares the tilt[2] from the HWRF forecast against the observations in the pre-RI and RI stages. As shown in Fig. 4a, the observed tilt (measured by the circulation displacement between 2 km and 8 km) is towards the southeast in the pre-RI stage with 75-km magnitude, while the corresponding RMW at the surface is only about 50 km. According to Chen and Fang (2012), such a tilt/RMW configuration will lead to the deep convection falling outside of the RMW and, subsequently, the diabatic heating efficiency should be significantly diminished. However, a major concern about using the surface RMW in evaluating the efficiency of diabatic heating is that the maximum diabatic heating usually occurs in the middle and upper levels. For a highly sloped eyewall, the surface RMW might be significantly different from the RMW at the upper level. For this reason, a fixed radius was used instead of the surface RMW to evaluate the efficiency of diabatic heating. The wavenumber-1 asymmetry in the low-level wind field has the maximum wind speed located in the northeast quadrant (shaded) as a result of the northwestward translation of the storm. The wind field asymmetry and the vortex tilt from the HWRF forecast (Fig. 4b) resemble the Doppler observed structure very well. The tilt in the RI stage (i.e., 9 h after RI onset) rotates anticyclonically and becomes much smaller for both the observations and HWRF forecast. The shear, 6.5-7 m s^{-1} at this time, is greater than the shear in the later time of pre-RI period for the HWRF forecast, suggesting the tilt magnitude is more likely determined by the ratio of shear to storm intensity instead of shear magnitude alone. For a given amount of

[2] For the purpose of comparison with observations, we have computed the tilt using earth-relative flow in this section.

shear, a weaker storm will respond with larger tilt, while a stronger storm will be more resilient to the shear and exhibit less tilt.

5. Storm structure evolution

Figure 4 shows that tilt is large in the pre-RI stage and reduces during the RI stage. Previous studies have shown that RI onset is associated with a vertical alignment of the vortex (e.g., Chen 2012). To examine if vortex alignment is the trigger for the RI of Hurricane Earl, the hourly tilt hodograph from 48 h (i.e., 9 h prior to RI onset) to 66 h (i.e., 9 h after RI onset) is depicted in Fig. 5. The tilt is northeastward at 48 h with 41 km magnitude, rotating clockwise to the south as its magnitude shrinks significantly to 22 km at 51 h. The tilt vector then rotates cyclonically while its magnitude increases to 50 km at 57 h when RI commences. It continues to rotate cyclonically, but magnitude rapidly decreases after 58 h. Within this 18-h period the minimum tilt is 10 km, which occurs at 65 h (i.e., 8 h after RI onset). In general, the tilt decreases with intensification as shown in Figs. 4 and 5, but the tilt at RI onset (i.e., t = 57 h) is still large. The tilt precession shown in Fig. 5 demonstrates that vertical alignment is the result instead of the trigger for RI. Nevertheless, Earl does become vertically aligned in the later RI stage despite its highly asymmetric convective distribution.

6. The upper level warming

The accelerated deepening of central pressure is associated with a sudden temperature change in the eye center, caused by either an abrupt increase in magnitude as demonstrated in the idealized numerical study of Gopalakrishnan et al. (2011) or by a sudden elevation of the warm core height. Chen and Zhang (2013) showed that the RI onset of Hurricane Wilma (2005) was associated with the warm core being elevated from 12 km to 14 km altitude; however, in those studies, this did not occur until the vortex became horizontally symmetric and vertically aligned.

To examine if Earl's RI occurred due to the warm core shifting upward, *despite its significant horizontal asymmetry and vertical tilt*, the time-height cross section of temperature perturbation with respect to the 400 km × 400 km domain averaged temperature profile at forecast initial time is plotted in Fig. 6a. As observed, there is a stark difference between the pre-RI and RI stages similar to what is shown in Zhang and Chen (2012). The warming is focused below 8 km in the pre-RI stage and then suddenly extends to 14 km in the RI stage with maximum warming setting in at 8 km altitude at the end of the forecast.

To quantify the contribution of the warming above 8 km to the surface pressure change, a hydrostatic calculation is performed by removing the warming above 8 km, and the result is plotted in Fig. 6b. The original surface pressure is also plotted for the purpose of comparison. It can be seen that RI would not have occurred and that the final central pressure would have been 45 hPa higher without the warming above 8 km. This figure clearly demonstrates that warming in the upper level (i.e., above 8 km) resulted in the RI of Earl.

One question spontaneously rises: what causes the warming above 8 km? Zhang and Chen (2012) explained that the upper-level warming development in Hurricane Wilma (2005) was due to compensating subsidence from CBs trapped in the inner core region due to weak, storm-relative flow in the eye and large inertial stability associated with the development of the symmetric eyewall. However, Hurricane Earl never achieved a fully symmetric eyewall in this 120-h forecast, and there is northerly flow across the storm center at 8-km altitude as shown in Fig.5 at 60 h. Apparently, the development of upper-level warming in Earl was very different from that in Hurricane Wilma.

Previous studies (Nolan et al. 2007; Vigh and Shubert 2009; Rogers et al. 2013) have already pointed out that CBs taking place inside the RMW are more efficient in spinning up the vortex. To test this hypothesis, a time series of CB[3] numbers in the first 72 h stratified by the radius (i.e., r ≤ 50 km, 50 km ≤ r ≤ 100 km, 100 km ≤ r ≤ 150 km, 150 km ≤ r ≤ 200 km) is shown in Fig.7a. Fixed radii are used instead of the RMW because the RMW as shown in Fig. 1c exhibits large fluctuations, especially in the early hours of the forecast. Time series of shear magnitude, central pressure, and maximum surface wind are also plotted in Fig. 7a to facilitate viewing the relationship between them and CB activity. While CBs inside 50 km are considered as being in a favorable region for intensifying the vortex, most CBs fall within the 50-150 km radius. In general, the number of CBs at all radii exhibit episodic behavior at irregular intervals.

Moon and Nolan (2010) pointed out that Convective Available Potential Energy CAPE in the environment needed to be restored to support a new CB episode, after a previous CB episode exhausted the CAPE. There are three major episodes in the pre-RI stage (i.e., prior to 57 h): 9-15 h, 24-30 h, and 36-42 h. The first two episodes occur when the shear magnitude is < 4 m s^{-1}, and the third episode occurs when the shear increases to near 6 m s^{-1}. Figure 7a shows that the surface wind speeds respond to each episode with dramatic fluctuations, increasing rapidly when the CB episode starts picking up and weakening quickly when the episode starts to die down. In the second episode, the surface wind speed increases from 20 m s^{-1} to 28 m s^{-1} from 24 h to 27 h then rapidly returns to its pre-episode value at the end the episode. However, at the end of the third episode, there is a net 3 m s^{-1} increase in the wind speed. Starting at 53 h, the surface wind speed shows a steady increase with small fluctuations as the shear increases from 5 m s^{-1} to 6.8

[3]A convective burst is defined as a grid point with its maximum vertical motion greater than 3ms^{-1} in the column.

m s^{-1}. In contrast to the surface wind response to the CB episodes, central pressure does not show a similar response, yet it does begin to deepen continuously after 52 h (i.e., 1 h prior to the surface wind increases).

Based on this fine scale analysis of the time series of central pressure and surface wind, it seems the RI onset should be flagged at 52 or 53 h. However, as pointed out in section 4, the deepening rate is still only about 0.1 hPa h^{-1} around this time. Nevertheless, the 52-57 h time period into the forecast can be viewed as a pre-conditioning stage for RI. How the pre-conditioning process occurs is not yet clear in Fig. 7a. The evolution of CBs occurring near the center (i.e., $\leq$ 50 km radius) does not appear to be closely related to intensity change, which implies diabatic heating close to the center is an insufficient condition for RI in the case of Earl.

To examine the possible relationship between CB azimuthal distribution and intensity change, Fig. 7b shows a similar time series to Fig. 7a, but the CBs are stratified by the shear-oriented quadrants instead of the radius. The evolution of CBs in Fig. 7b is very similar to Fig. 7a before 50 h with periodic CB episodes occurring randomly in different quadrants. However, CBs in the downshear-left (red line) dominate after 50 h, and this downshear-left dominance pattern persists until 72 h. The central pressure and surface wind speed start to intensify continuously a couple of hours after the downshear-left dominance pattern occurs, which indicates downshear-left is a favorable quadrant for CBs to intensify the storm. Downshear-left CB episodes occur prior to 50 h, but there are two major differences between those episodes and the episode after 50 h. First, there are many other CBs taking place in other quadrants which make downshear-left CBs much less distinct. This suggests downshear-left dominance of CB distribution might be one of the necessary conditions for the RI of Earl. Second, the duration of downshear-left CBs is shorter than the episode after 50 h, which suggests the persistence of CBs is also important, consistent with previous studies (e.g., Nolan et al. 2007, Cecelski and Zhang 2013).

The CB distribution is further refined by shear-oriented quadrants within a 50-km radius to consider both the radius and azimuthal factors. As shown Fig. 7c, there are two distinct episodes in the downshear-left quadrant with the second episode dominating all other quadrants, although its duration is shorter than that in Fig. 7b. Fig. 7c suggests that both the radius and shear-oriented direction are important in determining the efficiency of CBs to spin up the vortex.

Figure 7 shows that there is a relationship between CB activity and intensity change, especially when the CBs are measured in shear-oriented quadrants. But exactly how are they related? As shown in Fig. 6a, RI onset is related to sudden warming in the upper troposphere of the eye center. Subsidence in the hurricane eye is well recognized as the mechanism responsible for the formation of the warm core, but such a mechanism has remained enigmatic since this branch of circulation consumes energy produced elsewhere in the hurricane.

Previous studies have put forward a few hypotheses. Using an axisymmetric vortex model, Smith (1980) demonstrated that subsidence warming in the eye was mechanically driven by decreasing tangential winds in the vertical as a consequence of thermal wind balance. Willoughby (1998) viewed subsidence as the result of RMW contraction as the storm intensified. To examine the relationship between subsidence in the inner core and intensity change, shear-oriented subsidence averaged from surface to 12-km altitude inside the 50-km radius is shown in Fig. 8. The subsidence in each quadrant between 24-39 h is quite vigorous, with multiple peaks up to 0.3 m s^{-1} that occur periodically, similar to the CBs in Fig. 7b. The subsidence in all quadrants is relatively weak between 39-50 h, after which there is sustained subsidence in the upshear-left quadrant. It appears from Figs. 7b and 8 that subsidence in the upshear-left quadrant is closely correlated in time to the CBs in the downshear-left quadrant. This is consistent with the results of Eastin et al. (2005) and Reasor et al. (2009), which showed the subsidence is maximized in the upshear region next to the down-shear left deep convection in Hurricane Guillermo (1997).

Figures 7 and 8 imply that RI onset is related to sustained convection in the downshear-left quadrant and subsidence in the upshear-left quadrant. To demonstrate how the downshear-left convection and upshear-left subsidence contribute to formation of the warm core and RI, Figs. 9a and 9c show the hourly averaged potential temperature anomaly (black contour) and vertical motion (shading) at 8-km altitude during RI pre-conditioning (i.e., 54-55 h) and RI onset (i.e., 57-58 h) stages, respectively. In Fig. 9a, the mesoscale vertical motion shows a wave number-1 asymmetry with ascent downshear and descent upshear. Superposed on this mesoscale vertical motion distribution is strong deep convection in the downshear-left quadrant and strong subsidence in the upshear-left quadrant next to downshear-left deep convection. The strongest subsidence is located along the downwind edge of deep convection. Associated with this distribution of vertical motion are two regions of warm anomaly, a broad one in the deep convection region with a maximum of 3 K and a narrow one in the subsidence region with a maximum of 2 K, separated by a cooling line (marked by a blue dashed line). The storm-relative circulation center at 8-km altitude ("×" mark in Fig. 9a) is located at the edge of downshear-left deep convection. This configuration allows flow at upper level advect the warm anomaly associated with subsidence in the upshear-left towards the low-level storm center and reduce the surface pressure, which suggest the horizontal advection may play an important role in the development of the upper-level warm core. The hourly averaged diabatic heating distribution is very similar to the vertical motion distribution with heating in upward motion area and cooling in downward motion area. Figure 9b shows the heating associated with deep convection in the downshear-left quadrant can be as large as 20 K hr^{-1}, 95% of which is offset by the adiabatic cooling. Right next to the strong diabatic heating is strong evaporative cooling which is up to 10 K hr^{-1} and is responsible for the cooling line seen in Fig. 9a. However, it is important to note that despite a cooling trend due to microphysical processes at the downstream of the cooling line (Fig. 9a), it can't offset the warming produced by subsidence further downstream resulting in net warming (Fig. 9a).

3 h later (Fig. 9c), the deep convection area has expanded significantly and is located farther northeast with part of the deep convection occurring in the upshear-left quadrant. The warm anomaly region in the upshear left at this time becomes much more significant in terms both coverage and magnitude compared to 3 h earlier. Therefore, the horizontal temperature advection is much more significant at this time. Fig. 9d showed corresponding diabatic heating distribution which is very similar to Fig. 9b with strong diabatic heating associated with deep convection in the downshear left and evaporative cooling next to it responsible for the cooling line.

Figure 10 shows the azimuth-height cross section of vertical motion averaged between 50-km radius and 100-km radius during pre-conditioning stage and RI onset. As it can be seen, all the deep convection concentrates in downshear region with most of it in downshear-left in the pre-conditioning stage (Fig. 10a). Compared to the upward motion, the downward motion shows more characteristics. There is a strong convective-scale downward motion labeled "A" at the downstream of deep convection in the downshear-left quadrant. Near the edge of deep convection and below the melting level, this convective-scale downward motion is greatly enhanced by the evaporation. This distinct feature is consistent with earlier studies of Liu et al. (1999). The strong evaporation-driven downward motion below the melting level also indicates that the cells have entered a mature stage. Also the broad mesoscale subsidence in the upshear labeled “B”, which is the result of interaction between shear and vortex, occupies between 3 km and 10 km at this time and is enhanced by the convective-scale subsidence at the downstream of deep convection. Higher up, there is another kind of subsidence labeled “C” which results from the detrainment of stratospheric air due to the overshooting deep convection. This feature has also been documented by numerous studies (e.g. Velden and Smith 1983; Foley 1998). The detrainment subsidence is unlikely to play a major role in the development of upper-level warm core in this case since it is located in the upstream of deep convection.

3 h later, the deep convection rotates cyclonically and a small portion of deep convection occurs in the upshear-left. The deep convection at this time is more upright in comparison with slanted updraft in Fig. 10a. Lack of significant evaporation-driven downdraft below the melting level indicates that the convective cells are at its growing stages. Nevertheless, there is still convective-scale downward motion at the downstream of deep convection in the upshear-left quadrant (marked “A” in Fig. 10b). The broad mesoscale subsidence shown in Fig. 10a now extends vertically occupying between 2 km and 12 km. Consistent with Fig. 9c, the maximum warming is slightly downstream of maximum convective-scale downward motion in the upshear-left. Higher up, the detrainment subsidence is still located at the upstream of deep convection but it is stronger than 3 h earlier. This is consistent with the more upright deep convection at this time.

To further examine the role of horizontal temperature advection in the development of the warm core, the averaged temperature local tendency and horizontal temperature advection within the eye (i.e., radii ≤ 15 km) in the 8-14 km layer is calculated and shown in Fig. 11. The horizontal temperature advection is very close to the local tendency in the pre-RI stage and almost identical to the local tendency in the period between RI onset and vertical alignment. (i.e., 57-65 h). Once the vortex became vertically aligned, there are large differences between the temperature tendency and the horizontal advection, which implies the mechanism for warm core development prior to vertical alignment and after vertical alignment are different. This suggests that the balanced subsidence warming dictated by the thermal wind relationship proposed by Smith (1980) and the forced subsidence as a result of storm contraction proposed by Willoughby (1998) might be more applicable to a vertically-aligned vortex instead of a tilted vortex. Since horizontal warm air advection contributes to the development of the warm core, the warm core will not be the result of a passive response to the primary and secondary circulations. When there is sustained warming caused by horizontal warm advection occurring in the upper troposphere as shown in Figs. 7 and 8, the surface pressure will respond in a steady sense and allow for the gradient wind adjustment to occur and the subsequent wind speed to increase (Fig. 7).

7. Why does RI occur at that specific time?

We illustrated in section 6 that subsidence warming in the upshear-left quadrant is advected to the storm center and contributes to the development of an upper-level warm core. However, Fig. 7 shows that CBs occur almost all the time in the pre-RI stage and that they are even more vigorous between 24-42 h, yet RI occurs much later. Fig. 7b provides a hint that persistent downshear-left dominance of CBs is the key. Why does the downshear-left region need to be dominant? What do CBs do in different quadrants?

It is well known that TCs that evolve in a sheared environment tend to produce organized convection in the downshear region and subsidence in the upshear region (e.g., Jones 1995). This scenario is also depicted in the forecast of Hurricane Earl by the HWRF system (Figs. 9). The process of RI in sheared storms may be viewed as a mechanism of cooperative interaction between large/mesoscale subsidence in the upshear region and subsidence produced by convective elements that form first in the downshear left quadrant and then move cyclonically to the upshear quadrant, moistening the environment downstream near the low-level storm center. However, the scale, frequency, and, above all, location of these CBs appear to play a key role in the RI process. For the configuration to favor RI in a titled vortex, it must allow for the maximum subsidence-induced warming to be advected over the low-level storm center.

To examine the difference between CBs occurring in the four shear-oriented quadrants, Fig. 12 shows the schematic configuration of convective scale vertical motion and shear-induced mesoscale motion. The black arrow indicates shear direction. The light blue and red hemispheres denote the shear-induced mesoscale subsidence and ascent, respectively, which are weak but balanced. The red circle indicates aggregated CBs, and the dark blue ring surrounding it shows the convective-scale subsidence. Compared to mesoscale vertical motion, the convective-scale vertical motion is strong but unbalanced. The thick blue arrow indicates the horizontal temperature advection associated with the net subsidence warming determined by mesoscale subsidence and convective-scale subsidence. The magnitude of advection is presented by the color of the arrow with dark blue representing a larger magnitude. As can be seen, when CBs occur in the downshear-left and upshear-left quadrants (Figs. 12a and 12b), convective-scale subsidence induced at the downstream by the CBs is superposed on the mesoscale descent in the upshear region, and the net effect of the warming will be amplified, consistent with Reasor et al. (2009).

Compared to the favorable configuration just identified, upshear-right and downshear-right CBs produce subsidence in the mesoscale ascent region, which will offset the convective scale subsidence warming and are not favorable for RI (Figs. 12c and 12d). The animation of temperature horizontal distribution indicates that the warming in the downshear region does not accumulate; it only accumulates when sustained CB activity occurs in the downshear-left quadrant. This schematic figure also shows that the tilt magnitude/RMW configuration plays an important role. When the tilt is much larger than the surface RMW, the maximum warming may occur farther radially outward and will not be advected across the low-level storm center by the upper-level circulation to reduce the surface pressure in the most efficient way. Therefore, both the radial location and azimuthal location are important for CBs to intensify the vortex efficiently.

The schematic image shown in Fig.12 is predicated on the assumption that upper-level circulation is determined by the location of deep convection, which is the case when CBs are clustered in one quadrant instead of being scattering. For example, the vortex shows upshear tilt when most of the CBs occur in the upshear quadrants at 27 h. The tilt becomes southeastward when sustained downshear-left CBs dominate after 50 h. Zhang and Tao (2013) demonstrated that tilt is determined by deep convection when there is significant convection asymmetry. When CBs are scattered, each CB element competes with the others to become the new circulation center and the upper-level circulation is disorganized. Hence, a cooperative configuration between mesoscale subsidence in the upshear region and organized convection is required for RI.

Although deep convection in left of shear is shown to be more favorable for RI, random convective bursts do contribute to RI by moistening the vortex environment and allowing deep convection in the downshear-left quadrant take place persistently. As shown in Figure 13, the peak of relative humidity is a few hours later than the peak convective bursts activity for each CB episode, suggesting convective bursts moisten the environment. After the first three convective bursts episodes which do not contribute to the development of upper-level warm core and RI directly, relative humidity increased from 60% to more than 70%. What drives these CB episodes is one of our future research topics.

8. Concluding remarks

- For the first time the asymmetric, three-dimensional, rapid intensification of a tropical cyclone, Hurricane Earl (2010), is simulated using the operational, ocean-coupled, HWRF modeling system and verified not only with best track estimates, but also against inner core observations which were available especially during the pre-conditioning and RI stages of the storm.
- Apart from the routine track and 10-m wind speed, the model reproduced some salient, observed features of a sheared vortex such as the asymmetric convective pattern and tilt of the storm both at the pre-conditioning and RI stages for the Earl case. The size prediction, in terms of the RMW, especially after the initial spin up process, was close to the observation. We believe that in the absence of high-resolution observations in space and time this forecast is useful in providing further insights on the RI process.
- Both the HWRF forecast and the observations indicate that strong convection is highly asymmetric in the pre-conditioning and RI stages with most of the strong convection concentrated in the downshear/downshear-left quadrants. In contrast, the vertical vortex tilt evolves from the large tilt in the pre-conditioning and early RI stages to almost vertically aligned in the later RI stage.

- The hourly hodograph of vortex tilt from the HWRF forecast reveals that the tilt is still large when RI starts at 57 h, and begins to decrease rapidly, suggesting that vertical alignment of the vortex is the result of RI rather than the trigger.
- Analysis of the 2-min HWRF forecast output shows that, despite the asymmetry in convective activities, RI onset is associated with a sudden warming in the upper troposphere above the 8-km altitude, without which RI would not have occurred, and the final pressure would be as much as 45 hPa higher.
- An in-depth analysis reveals that the pre-conditioning and RI stages are associated with most of the deep convection within 200 km of the low-level center occurring in the downshear-left quadrant, which produces convective-scale subsidence warming in the upshear region where mesoscale subsidence warming is located. This scenario is similar to the observational study of Hurricane Guillermo (1997) depicted in Eastin et al. (2005). The maximum warming is caused by cooperative interaction between the convective-scale subsidence and shear-induced mesoscale subsidence. This warming is advected towards the low-level storm center by the upper-level circulation. If strong convection persistently occurs in the downshear-left quadrant, the horizontal advection of induced warming downstream of the evaporative cooling can play an important role in developing the upper-level warm core, lowering the surface pressure efficiently, and initiating RI. When strong convection is scattered randomly in different quadrants, each CB element competes with the others to become the new circulation center, and the beneficial collaboration between the upper-level flow field, convective-scale warming, and mesoscale warming as discussed above will not be realized. Nevertheless, some of the random CBs are found to moisten the environment near the vortex, providing a pre-cursor for RI process.

- The analysis also shows that wind speed increases when CB activity becomes vigorous. Yet, the wind speed only intensifies temporarily without the warming having developed in the upper level as a result of CBs occurring in the optimum quadrants. Therefore, we propose that RI onset and the early hours of RI occur in such a way that the wind adjusts to surface pressure changes caused by the upper-level warming which results from the horizontal advection of subsidence warming to the low-level center.
- It should be emphasized that although cloud-resolving models show some promise in RI predictions for individual cases, there is much less skill in forecasting intensity with fidelity over several TC forecasts. Both storm-to-storm and cycle-to-cycle variability are not uncommon. For instance, while the overall predictions of the intensification for the Earl case were reasonable, even the subsequent forecast cycle produced a delayed intensification. Additionally, while the current cycle of HWRF retrospective forecast reproduced the RI of Earl well, after the RI (after about 96 h into the forecast) there were some differences in minimum sea-level pressure with the observed central pressure deepening much faster until 108 h and then filling while the HWRF forecasted central pressure kept deepening. It is unclear at this time if these differences are due to an eyewall replacement cycle which is known to have predictability issues in numerical models. Our preliminary analysis, based on some of the surface wind behavior, shows that the HWRF system did not capture this subtle change, at least in this particular cycle. All these issues raise an important question on the predictability of convection, even in an organized system such as a hurricane. The HWRF system has been run in operations at cloud-permitting scales for a couple of seasons over the North Atlantic and Pacific basins and over the North Indian Ocean. Retrospective runs have also been made over several seasons. The challenge is to diagnose a good versus bad forecast

and address some of the predictability issues. We believe the current work provides a basis to address these issues. Studies in this direction are ongoing.

Acknowledgments. The authors acknowledge funding from NOAA's Hurricane Forecast Improvement Program (HFIP) that supported this work. We acknowledge the contributions from Drs.Thiago Quirino and Xuejin Zhang on the HWRF developmental efforts. Thanks are also due to Drs. Paul Reasor, Frank Marks, Robert Rogers and Tomi Vukicevic for providing a thorough internal review and insightful comments that led to significant improvements of the original manuscript. Thanks are due to Ms. Gail Derr for offering editorial support and to Mr. Josh Alland, a summer intern for analyzing some of the HWRF forecasts that led to this effort.

References

Cangialosi, J. P., 2010: Tropical cyclone report Hurricane Earl, 25 August–4 September 2010. NOAA/NHC, 279 pp. [Available online at http://www.nhc.noaa.gov/pdf/TCR-AL072010_Earl.pdf.]

Cangialosi, J. P., and J. L. Franklin, 2011: 2010 National Hurricane Center forecast verification report. [Available online at http://www.nhc.noaa.gov/verification/pdfs/Verification_2010.pdf.]

Cangialosi, J. P., and J. L. Franklin, 2012: 2011 Atlantic and eastern North Pacific forecast verification. 66th Interdepartmental Hurricane Conference, Charleston, SC, 5 March 2012. [Available on-line at http://www.ofcm.gov/ihc12/Presentations/01b-Session/03IHC_2012_Verification_(2012)_v2.pdf]

Cecelski, S., and D.-L. Zhang, 2013: Genesis of Hurricane Julia (2010) within an African Easterly wave: Low-level vortices and upper-level warming. *Journal of the Atmospheric Sciences*, **70,** 3799-3817.

Chen, H., D.-L. Zhang, J. Carton, and R. Atlas, 2011: On the rapid intensification of Hurricane Wilma (2005). Part I: Model prediction and structural changes. *Wea. Forecasting*, **26,** 885-901.

Chen, H., and D.-L. Zhang, 2013: On the rapid intensification of Hurricane Wilma (2005). Part II: Convective bursts and the upper-level warm core. *J. Atmos. Sci.*, **70,** 146-172.

Chen, Q., and J. Fang, 2012: Effects of vertical wind shear on intensity and structure of tropical cyclone. *J. Tropical Meteor.*, **18,** 172-186.

Corbosiero, K. L., and J. Molinari, 2002: The effects of vertical wind shear on the distribution of convection in tropical cyclones. *Mon. Wea. Rev.*, **130,** 2110–2123.

Eastin, M. D., W. M. Gray, and P. G. Black, 2005: Buoyancy of convective vertical motions in the inner core of intense hurricanes. Part II: Case studies. *Mon. Wea. Rev.*, **133,** 209–227.

Emanuel, K.A., 1987: An air-sea interaction model of intraseasonal oscillations in the tropics. *J. Atmos. Sci.*, **44,** 2324-2340.

Ferrier, B. S., 1994: A double-moment multiple-phase four-class bulk ice scheme. Part I: Description. *J. Atmos. Sci.,* **51,** 249–280.

Frank, W. M., and E. A. Ritchie, 2001: Effects of vertical wind shear on the intensity and structure of numerically simulated hurricanes. *Mon. Wea. Rev.*, **129,** 2249–2269.

Foley, G., 1998: A marked upper tropospheric temperature anomaly observed by an aircraft near a thunderstorm over inland Western Australia. *Aust. Met. Mag.*, **47,** 321-326.

Goldenberg, B.S., S. G. Gopalakrishnan , X. Zhang, V. Tallapragada, S. Trahan, T. Quirino, F. Marks, and R. Atlas, 2014: The 2012 Triply Nested, High-Resolution Operational Version of the Hurricane Weather Research and Forecasting System (HWRF): Track and Intensity Forecast Verifications. To be submitted to *Wea. Forecasting.*

Gopalakrishnan, S. G., F. Marks, X. Zhang, J.-W. Bao, K.-S.Yeh, and R. Atlas, 2011: The experimental HWRF System: A study on the influence of horizontal resolution on the structure and intensity changes in tropical cyclones using an idealized framework. *Mon. Wea. Rev.*, **139,** 1762–1784.

Gopalakrishnan, S., Q.L. Liu. Q, T. Marchok, V. Tallapragada, M. Tong, R. Tuleya, R. Yablonsky, L. Bernardet. 2012: Hurricane Weather Research and Forecasting (HWRF) Model: 2012 Scientific Documentation. NCAR Development Tested Bed Center Report. Available online at: http://www.dtcenter.org/HurrWRF/users/docs/index.php.

Gopalakrishnan, S. G., F. Marks, J. A. Zhang, X. Zhang, J.-W.Bao, and V. Tallapragada, 2013: A study of the impacts of vertical diffusion on the structure and intensity of the tropical cyclones using the high-resolution HWRF system. *J. Atmos. Sci.,* **70,** 524–541.

Hack, J. J., and W. H. Schubert, 1986: Nonlinear response of atmospheric vortices to heating by organized cumulus convection. *J. Atmos. Sci.,* **43,** 1559-1573.

Harnos, D. S., and S. W. Nesbitt, 2011: Convective structure in rapidly intensifying tropical cyclones as depicted by passive microwave measurements. *Geophys. Res. Lett.,* **38,** L07805, doi:10.1029/2011GL047010.

Hendricks, E. A., M. T. Montgomery, and C. A. Davis, 2004: The role of "vortical" hot towers in the formation of Tropical Cyclone Diana (1984). *J. Atmos. Sci.,* **61,** 1209–1232.

Hong, S.-Y., and H.-L. Pan, 1996: Nonlocal boundary layer vertical diffusion in a Medium-Range Forecast Model. *Mon. Wea. Rev.,* **124,** 2322–2339.

Jiang, H., 2012: The relationship between tropical cyclone intensity change and the strength of inner-core convection. *Mon. Wea. Rev.,* **140,** 1164–1176.

Jones, S. C., 1995: The evolution of vortices in vertical shear. I: Initially barotropic vortices. *Quart. J. Roy. Meteor. Soc.,* **121,** 821-851.

Kieper, M., and H. Jiang, 2012: Predicting tropical cyclone rapid intensification using the 37 GHz ring pattern identified from passive microwave measurements. *Geophys. Res. Lett.,* **39,** L13804,doi:10.1029/2012GL052115.

Liu, Y., D.-L. Zhang, and M. K. Yau, 1999: A multiscale numerical study of Hurricane Andrew (1992). Part II: Kinematics and inner-core structures. *Mon. Wea. Rev.,* **127,** 2597–2616.

Liu, Q., N. Surgi, S. Lord, W.-S. Wu, S. Parrish, S. Gopalakrishnan, J. Waldrop, and J. Gamache, 2006: Hurricane initialization in HWRF model. Preprints, 27th Conference on Hurricanes and Tropical Meteorology, Monterey, CA.

Molinari, J., P. Dodge, D. Vollaro, K. L. Corbosiero, and F. Marks, 2006: Mesoscale aspects of the downshear reformation of a tropical cyclone. *J. Atmos. Sci.*, **63,** 341–354.

Molinari, J., and D. Vollaro, 2010: Rapid intensification of a sheared tropical storm. *Mon. Wea. Rev.*, **138,** 3869–3885.

Montgomery, M. T., M. E. Nicholls, T. A. Cram, and A. B. Saunders, 2006: A vortical hot tower route to tropical cyclogenesis. *J. Atmos. Sci.*, **63,** 355–386.

Montgomery, M. T., J. A. Zhang, and R. K. Smith, 2013: An analysis of the observed low-level structure of rapidly intensifying and mature Hurricane Earl (2010). *Quart. J. Roy. Meteor. Soc.*, **138,** 1-18.

Moon, Y., and D. S. Nolan, 2010: The dynamic response of the hurricane wind field to spiral rainband heating. *J. Atmos. Sci.*, **67,** 1779-1805.

Nguyen, S. V., R. K. Smith, and M. T. Montgomery, 2008: Tropical-cyclone intensification and predictability in three dimensions. *Quart. J. Roy. Meteor. Soc.*, **134,** 563-582.

Nolan, D. S., Y. Moon, and D. P. Stern, 2007: Tropical cyclone intensification from asymmetric convection: Energetics and efficiency. *J. Atmos. Sci.*, **64,** 3377–3405.

Reasor, P., and M. D. Eastin, 2012: Rapidly intensifying Hurricane Guillermo (1997). Part II: Resilience in shear. *Mon. Wea. Rev.*, **140,** 425–444.

Reasor, P., M. T. Montgomery, and L. D. Grasso, 2004: A new look at the problem of tropical cyclones in vertical shear flow: Vortex resiliency. *J. Atmos. Sci.*, **61,** 3–22.

Reasor, P., M. D. Eastin, and J. F. Gamache, 2009: Rapidly intensifying Hurricane Guillermo (1997). Part I: Low-wavenumber structure and evolution. *Mon. Wea. Rev.*, **137,** 603–631.

Riemer, M., M. T. Montgomery, and M. E. Nicholls, 2010: A new paradigm for intensity modification of tropical cyclones: Thermodynamic impact of vertical wind shear on the inflow layer. *Atmos. Chem. Phys.*, **10,** 3163–3188, doi:10.5194/acp-10-3163-2010.

Rogers, R., S. Lorsolo, P. Reasor, J.Gamache, and F. Marks, 2012: Multiscale analysis of tropical cyclone kinematic structure from airborne Doppler radar composites. *Mon. Wea. Rev.*, **140,** 77–99.

Rogers, R., P. Reasor, and S. Lorsolo, 2013: Airborne Doppler observations of the inner-core structural differences between intensifying and steady-state tropical cyclones. *Mon. Wea. Rev.*, **141,** 2970–2991.

Sitkowski, M., and G. M. Barnes, 2009: Low-level thermodynamic, kinematic, and reflectivity fields of Hurricane Guillermo (1997) during rapid intensification. *Mon. Wea. Rev.*, **137,** 645–663.

Smith, R. K., 1980: Tropical cyclone eye dynamics. *J. Atmos. Sci.*, **37,** 1227–1232.

Tang, B., and K. Emanuel, 2010: Midlevel ventilation's constraint on tropical cyclone intensity. *J. Atmos. Sci.*, **67,** 1817–1830.

Velden, C. S., and W. L. Smith, 1983: Monitoring tropical cyclone evolution with NOAA satellite microwave observations. *J. Climate Appl. Meteor.*, **22**, 714–724.

Vigh, J. L., and W. H. Schubert, 2009: Rapid development of the tropical cyclone warm core. *J. Atmos. Sci.*, **66,** 3335-3350.

Willoughby, H. E., 1998: Tropical cyclone eye thermodynamics. *Mon. Wea. Rev.*, **126,** 3053-3067.

Yablonsky, R. M., and I. Ginis, 2008: Improving the ocean initialization of coupled Hurricane–Ocean models using feature-based data assimilation. *Mon. Wea. Rev.*, **136,** 2592–2607.

Zhang, D.-L., and H. Chen, 2012: Importance of the upper-level warm core in the rapid intensification of a tropical cyclone. *Geophys. Res. Lett.,* **39,** L02806, doi:10.1029/2011GL050578.

Zhang, F., and D. Tao, 2013: Effects of vertical wind shear on the predictability of tropical cyclones. *J. Atmos. Sci.,* **70,** 975–983.

Zhang, J. A., R. Rogers, P. Reasor, E. W. Uhlhorn, and F. D. Marks, 2013: Asymmetric hurricane boundary layer structure from dropsonde composites in relation to the environmental vertical wind shear. *Mon. Wea. Rev.,* **141,** 3968–3984.

Figure Captions

Figure 1: (a) HWRF-forecasted (red line) and observed track (black line) at 6-h interval; (b) time series of HWRF-forecasted (2-min-resolution; red line) and observed (6-h-resolution; black line) maximum surface wind (V_{max}, m s^{-1}) and central pressure (P_{min}, hPa) for the period of 26/18-00 to 31/18-120. For HWRF-forecasted pressure, a semidiurnal filter is applied to the central pressure time series (blue line) to remove storm-unrelated pressure change (red line); (c) time series of HWRF-forecasted (2-min-resolution; red line) and observed (6-h-resolution; black line) RMW (km). The black dashed line in (b) indicates RI onset.

Figure 2: Time series of (a) vertical wind shear between 850-200 hPa averaged within 1000 km × 1000 km; and (b) SSTs at the storm center for the HWRF forecast (red line) and GFS reanalysis (black line). The black and red dashed lines indicate RI onset for observation and HWRF forecast respectively.

Figure 3: (a) Lower fuselage radar observation of radar reflectivity at 2230 UTC 28 Aug; (b) HWRF forecasted radar reflectivity from the 29.5-h forecast (valid at 2330 UTC 28 Aug); (c) Lower fuselage radar observation of radar reflectivity at 1045 UTC 29 Aug; and (d) HWRF forecasted radar reflectivity from the 62.75-h forecast (valid at 0845 UTC 29 Aug). The black circles indicate the 50-km, 100-km, and 150-km radii, and the black arrow indicates the shear direction. Ticks are marked at the 36-km interval.

Figure 4: Wind speed (shading) at 2-km altitude and stream-line (grey lines) at 8-km altitude from (a) composite radar observation in the pre-RI stage; (b) HWRF forecast in the pre-RI stage; (c) composite radar observation in the RI stage; and (d) HWRF forecast in the RI

stage. The black circles indicate the 50-km, 100-km, and 150-km radii, and the black arrow indicates the tilt direction.

Figure 5: Hourly hodograph of tilt from 48-66 h. The blue circle depicts the 50-km radius, and the green arrow shows the northerly shear. They represent the mean RMW and shear direction within this 18-h period. The tilt is calculated as the horizontal displacement of storm-relative circulation centers at 2-km and 8-km altitude.

Figure 6: (a) Time-height cross section of temperature perturbation at the eye center of Earl with respect to the reference temperature profile defined as the 400 km × 400 km area-averaged mean temperature at the model initial time; and (b) Time series of central pressure from the whole column warming (red line) and the warming below 8 km (blue line). Black dashed line in (a) indicates RI onset and red dashed line in (a) shows the trend of warm core boundary.

Figure 7: Time series of 2-min-resolution central pressure (black line), shear magnitude (orange line), maximum surface wind speed (grey line), and CB number stratified by (a) radius $r \leq 50$ km, 50 km $\leq r \leq$ 100 km, 100 km $\leq r \leq$ 150 km, 150 km $\leq r \leq$ 200 km; (b) shear-oriented quadrants within a 200-km radius; and (c) shear-oriented quadrants within a 50-km radius for the first 72-h forecast. The shear magnitude is multiplied by 100, and the maximum surface wind is multiplied by 20 to fit the scale on the left axis for (a) and (b). The shear magnitude is multiplied by 20, and the maximum surface wind is multiplied by 4 to fit the scale on the left axis for (c).

Figure 8: Time series of subsidence averaged between 0-12 km within a 50-km radius for the first 72-h forecast for downshear-left (DSL), upshear-left (USL), upshear-right (USR) and downshear-right (DSR).

Figure 9: Hourly averaged vertical motion (shading) superposed with potential temperature anomaly (black contours at 0.5 K interval), shear vector (red arrows), and storm-relative flow vector (grey arrows) at 8-km altitude for (a) averaged between 54 – 55 h, corresponding to 0000-0100 UTC 29 Aug; and (c) averaged between 57 – 58 h, corresponding to 0300 – 0400 UTC 29 Aug. The white circle indicates the 50-km radius, and the blue dashed line indicates the cooling that separates diabatic heating from subsidence warming. The green cross indicates the circulation center at 8-km altitude. (b) and (d) show the hourly averaged diabatic heating for 54 – 55 h and 57 – 58 h respectively. The black contours show the zero vertical motion.

Figure 10: Azimuth-height cross section of ring-averaged (50 km ≤ r ≤ 100 km) vertical motion and time averaged between (a) 54 – 55 h and (b) 57 – 58 h. Blue letter “A”, “B” and “C” indicate convective-scale downward motion, shear-driven mesoscale downward motion and stratospheric detrainment downward motion, respectively.

Figure 11: Time series of horizontal advection of potential temperature (red line) and temperature local tendency (blue line) averaged over 8-14 km within a 15-km radius. Black dashed lines indicate the timing of RI onset and vertical alignment.

Figure 12: Schematic depiction of configuration of shear-induced mesoscale subsidence (light blue semicircle), mesoscale ascent (light red semicircle), CBs (dark red circle), and convective-scale compensated subsidence (dark blue ring). The black circle indicates the RMW at the surface, and the black arrow shows the shear direction (northerly shear). The thick blue arrow indicates the upper-level flow associated with CBs. For CBs located in (a) downshear-left and (b) upshear-left, convective-scale subsidence is superposed on the

mesoscale subsidence. For CBs located in (a) upshear-right and downshear-right, convective-scale subsidence is superposed on the mesoscale ascent.

Figure. 13: Time series of the number of CBs and domain averaged relative humidity (400 km × 400 km × 14 km).

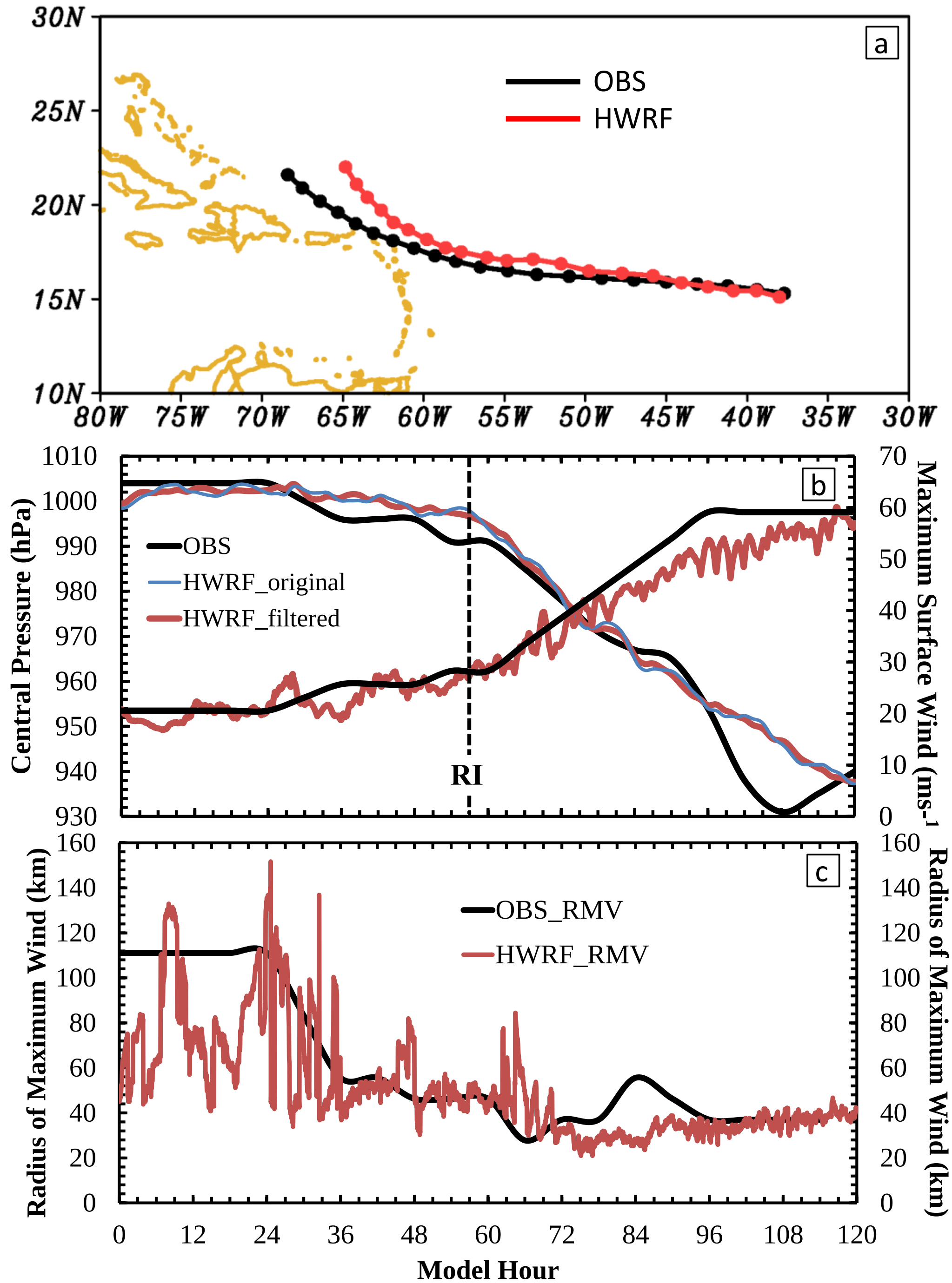

Fig. 1. (a) HWRF-forecasted (red line) and observed track (black line) at 6-h interval; (b) time series of HWRF-forecasted (2-min-resolution; red line) and observed (6-h-resolution; black line) maximum surface wind (V_{max}, m s^{-1}) and central pressure (P_{min}, hPa) for the period of 26/18-00 to 31/18-120. For HWRF-forecasted pressure, a semidiurnal filter is applied to the central pressure time series (blue line) to remove storm-unrelated pressure change (red line); (c) time series of HWRF-forecasted (2-min-resolution; red line) and observed (6-h-resolution; black line) RMW (km). The black dashed line in (b) indicates RI onset.

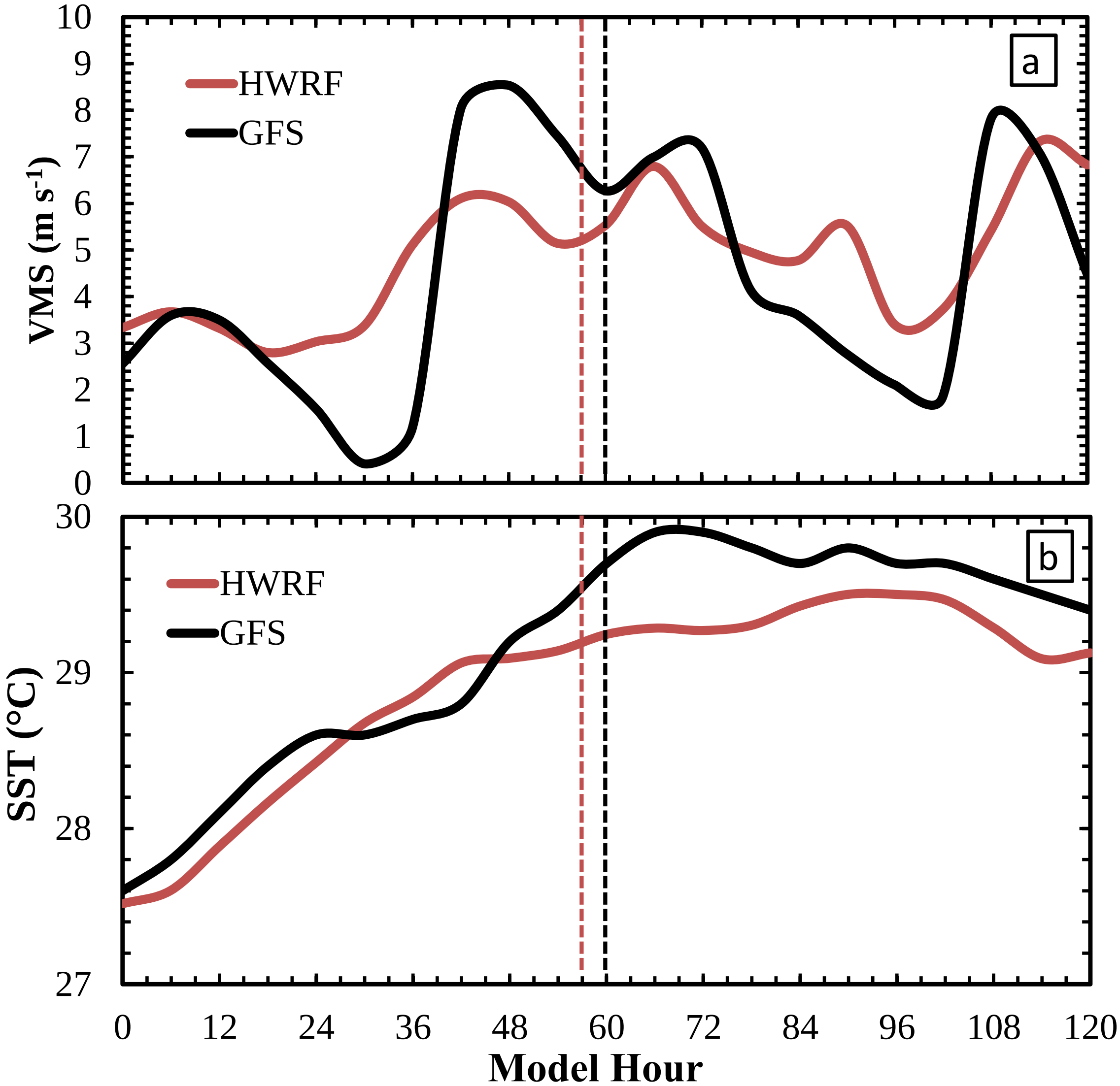

Fig. 2. Time series of (a) vertical wind shear between 850-200 hPa averaged within 1000 km × 1000 km; and (b) SSTs at the storm center for the HWRF forecast (red line) and GFS reanalysis (black line). The black and red dashed lines indicate RI onset for observation and HWRF forecast respectively.

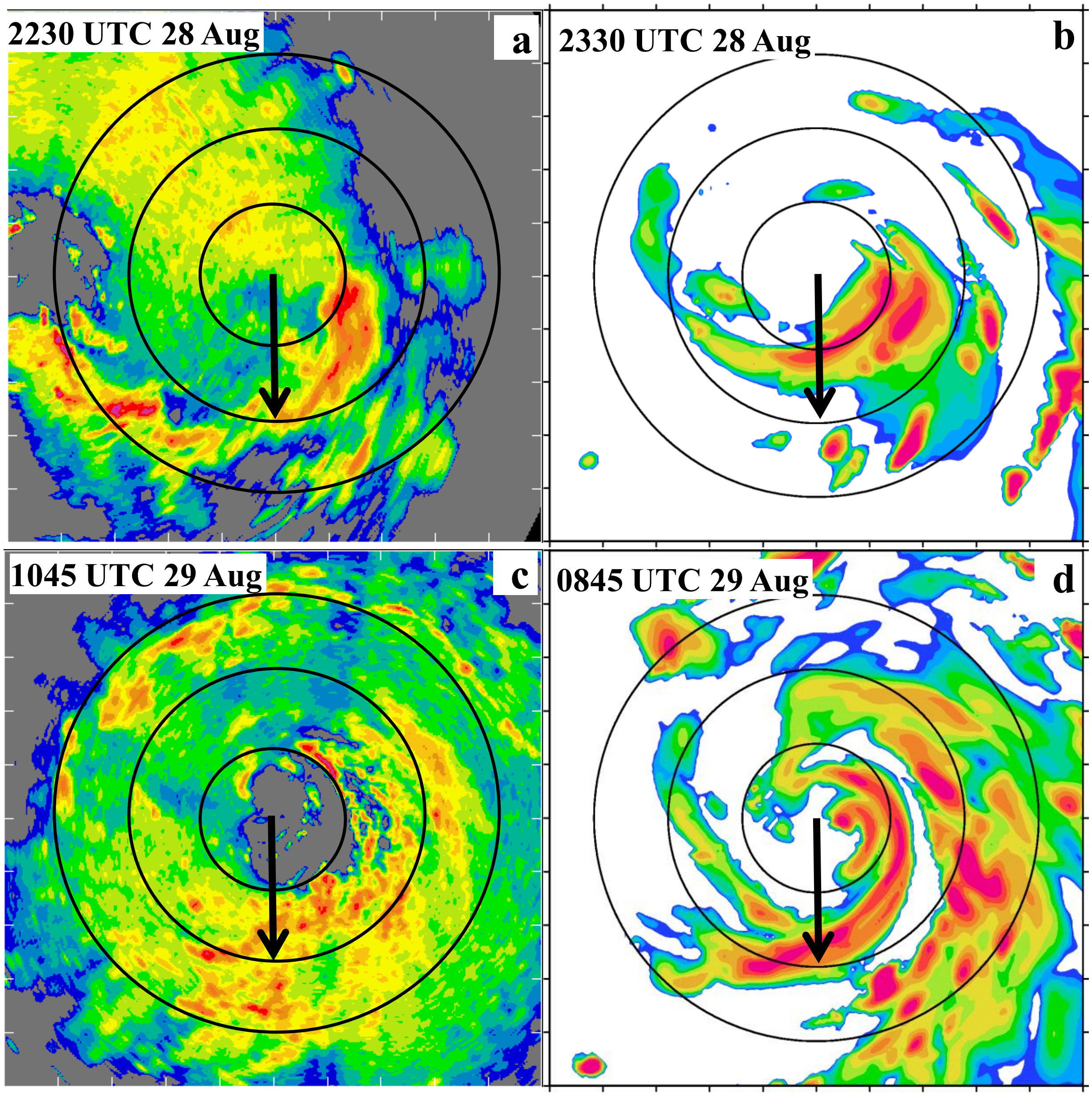

Fig. 3. (a) Lower fuselage radar observation of radar reflectivity at 2230 UTC 28 Aug; (b) HWRF forecasted radar reflectivity from the 29.5-h forecast (valid at 2330 UTC 28 Aug); (c) Lower fuselage radar observation of radar reflectivity at 1045 UTC 29 Aug; and (d) HWRF forecasted radar reflectivity from the 62.75-h forecast (valid at 0845 UTC 29 Aug). The black circles indicate the 50-km, 100-km, and 150-km radii, and the black arrow indicates the shear direction. Ticks are marked at the 36-km interval.

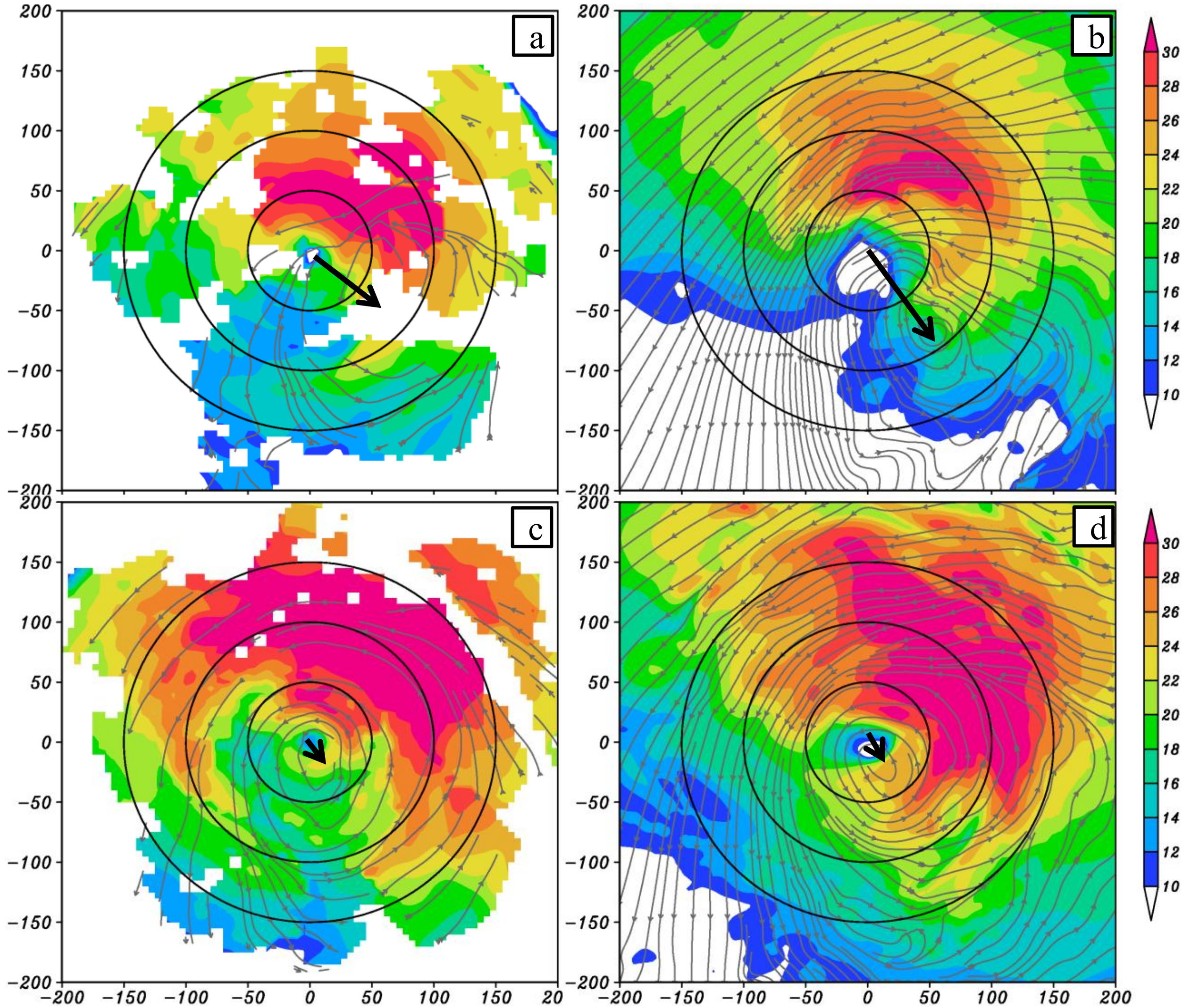

Fig. 4. Wind speed (shading) at 2-km altitude and stream-line (grey lines) at 8-km altitude from (a) composite radar observation in the pre-RI stage; (b) HWRF forecast in the pre-RI stage; (c) composite radar observation in the RI stage; and (d) HWRF forecast in the RI stage. The black circles indicate the 50-km, 100-km, and 150-km radii, and the black arrow indicates the tilt direction.

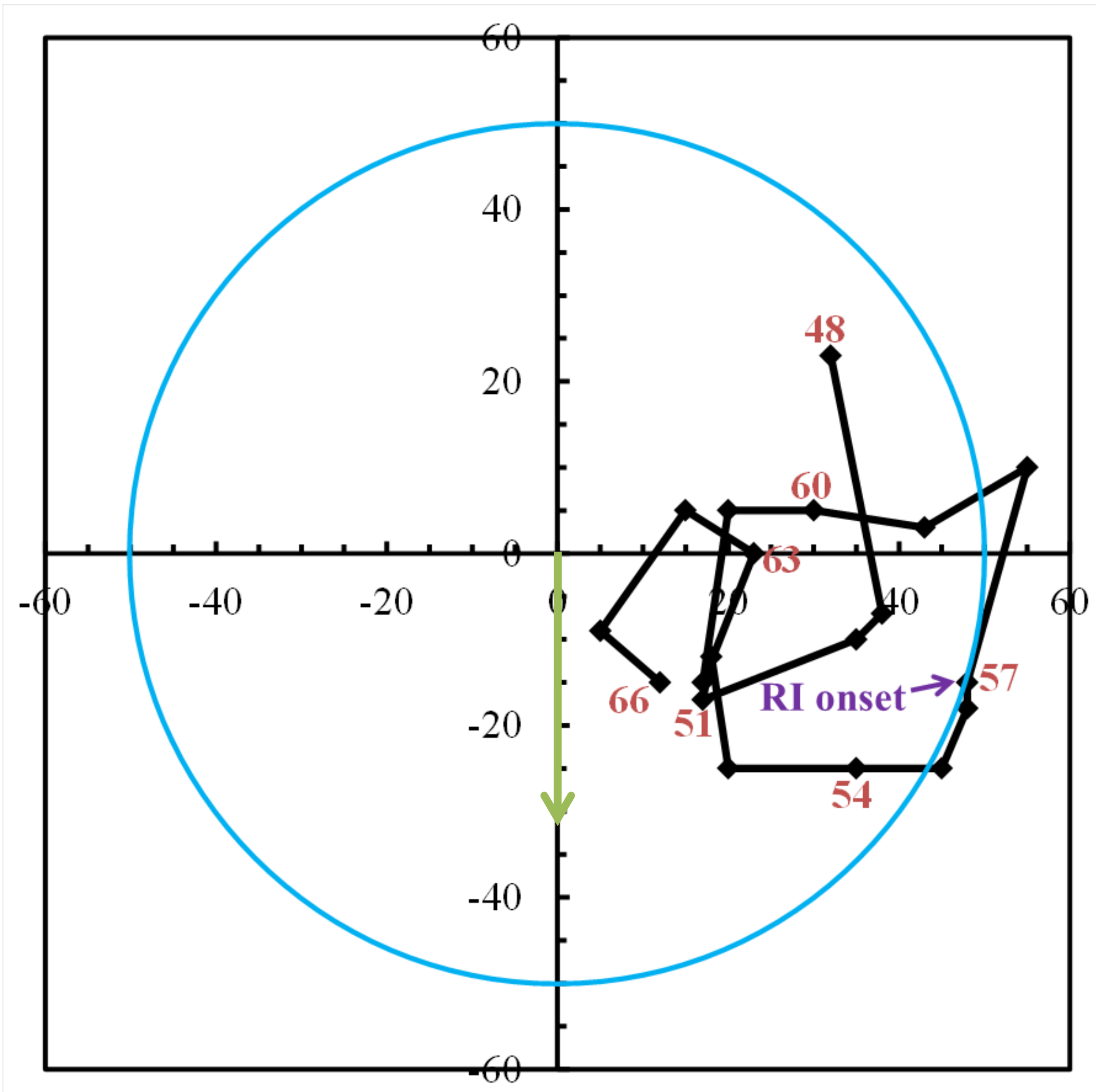

Fig. 5.Hourly hodograph of tilt from 48-66 h. The blue circle depicts the 50-km radius, and the green arrow shows the northerly shear. They represent the mean RMW and shear direction within this 18-h period. The tilt is calculated as the horizontal displacement of storm-relative circulation centers at 2-km and 8-km altitude.

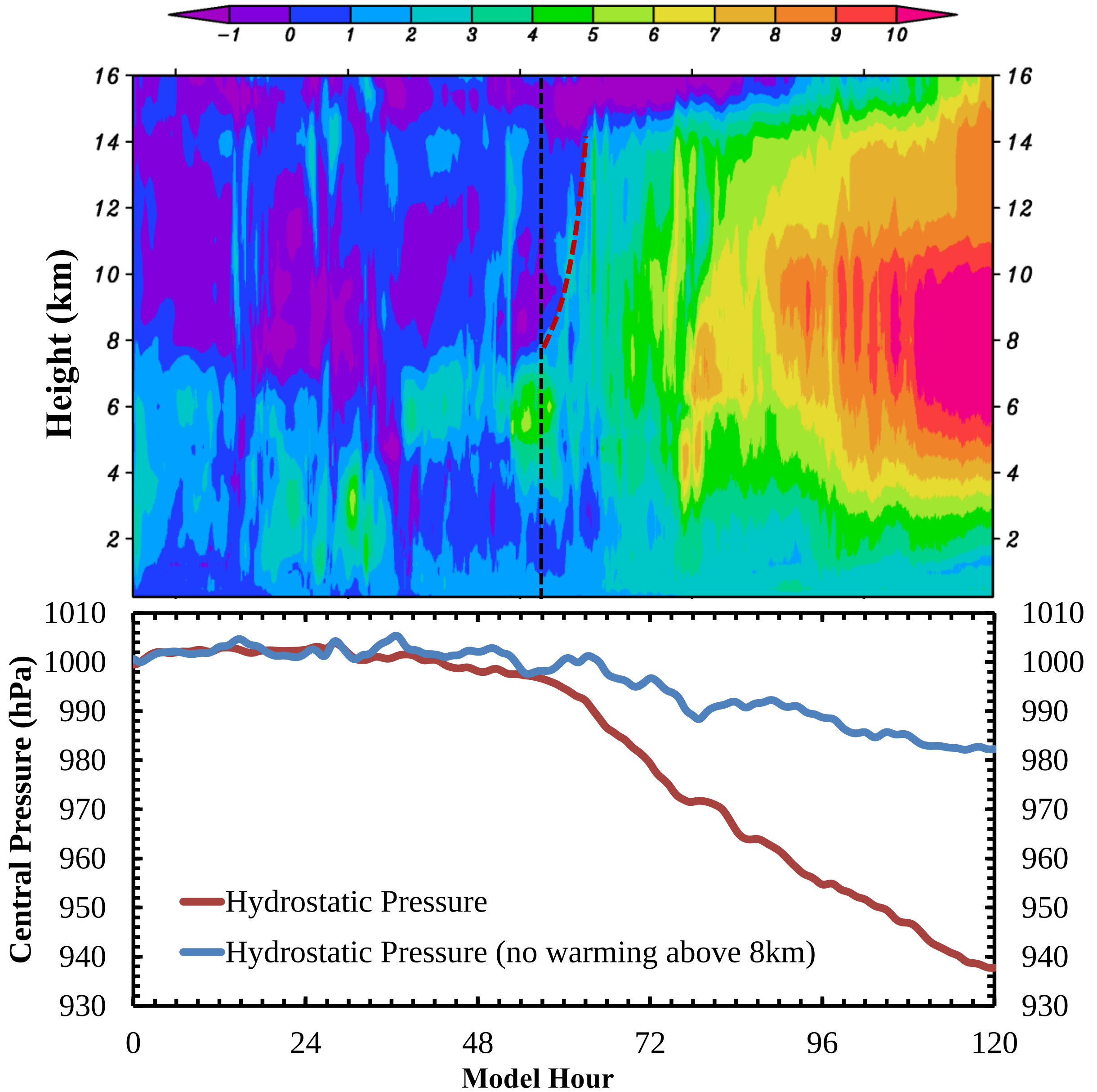

Fig. 6. (a) Time-height cross section of temperature perturbation at the eye center of Earl with respect to the reference temperature profile defined as the 400 km × 400 km area-averaged mean temperature at the model initial time; and (b) Time series of central pressure from the whole column warming (red line) and the warming below 8 km (blue line). Black dashed line in (a) indicates RI onset and red dashed line in (a) shows the trend of warm core boundary.

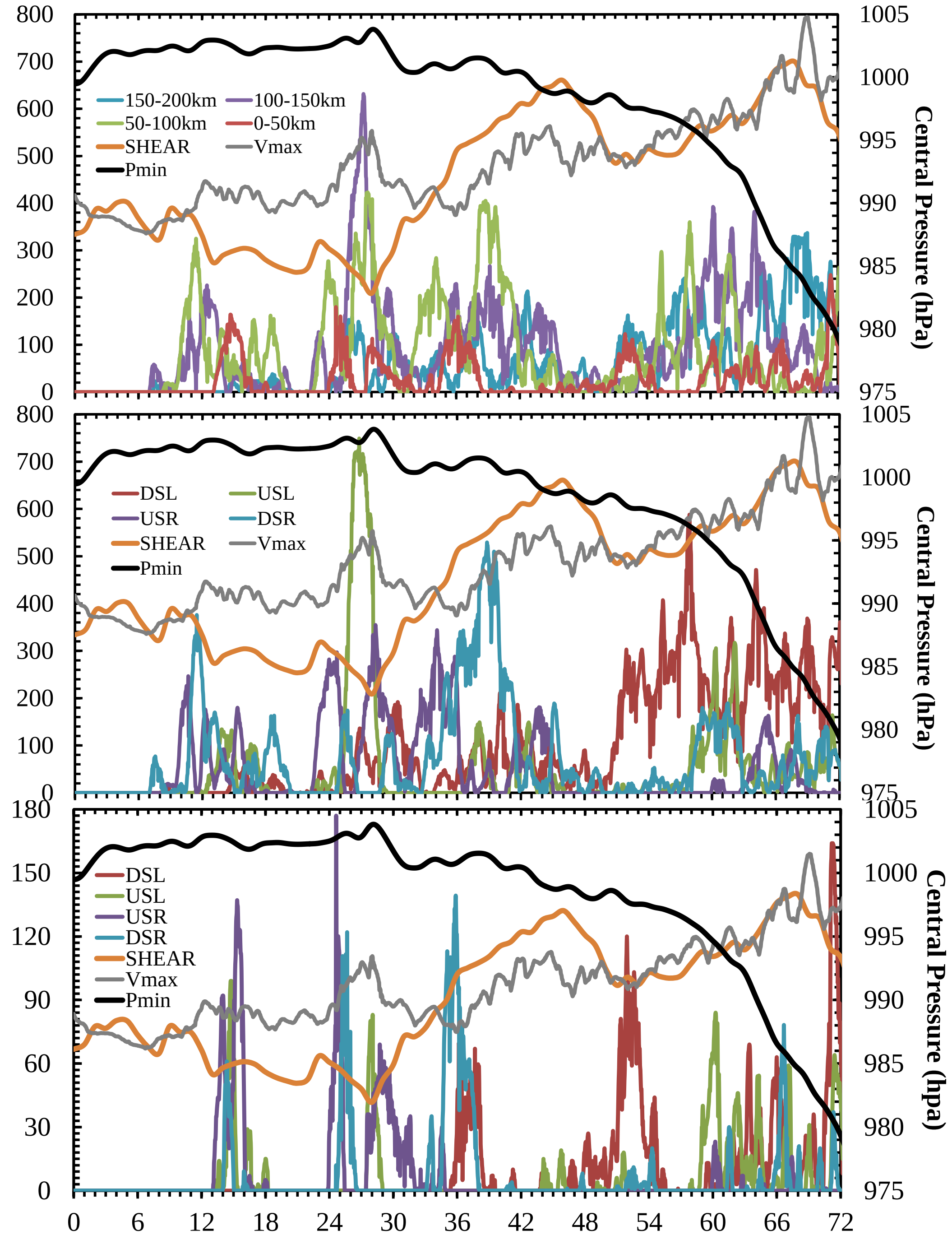

Figure 7: Time series of 2-min-resolution central pressure (black line), shear magnitude (orange line), maximum surface wind speed (grey line), and CB number stratified by (a) radius r ≤ 50 km, 50 km ≤ r ≤ 100 km, 100 km ≤ r ≤ 150 km, 150 km ≤ r ≤ 200 km; (b) shear-oriented quadrants within a 200-km radius; and (c) shear-oriented quadrants within a 50-km radius for the first 72-h forecast. The shear magnitude is multiplied by 100, and the maximum surface wind is multiplied by 20 to fit the scale on the left axis for (a) and (b). The shear magnitude is multiplied by 20, and the maximum surface wind is multiplied by 4 to fit the scale on the left axis for (c).

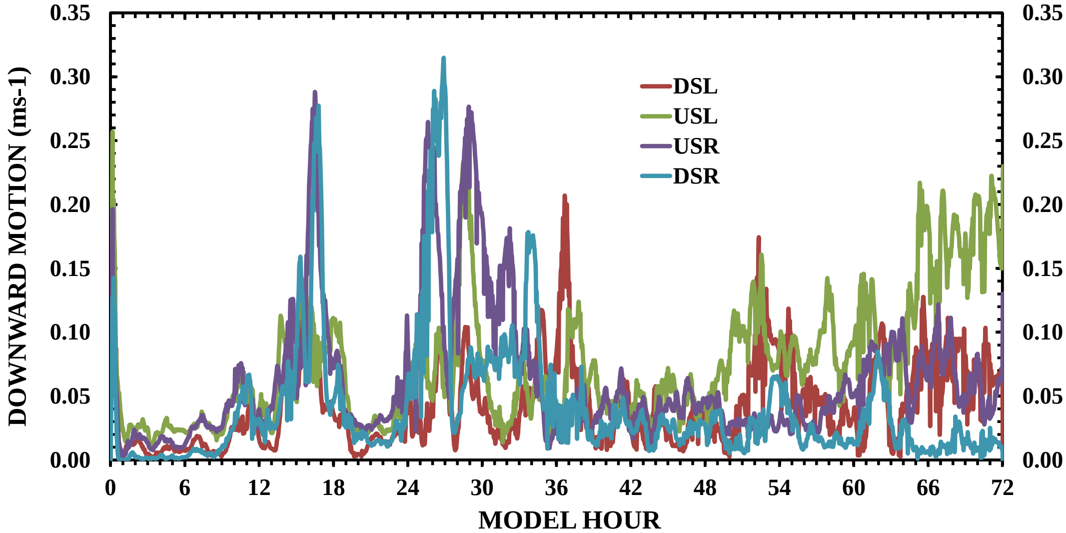

Figure 8: Time series of subsidence averaged between 0-12 km within a 50-km radius for the first 72-h forecast for downshear-left (DSL), upshear-left (USL), upshear-right (USR) and downshear-right (DSR).

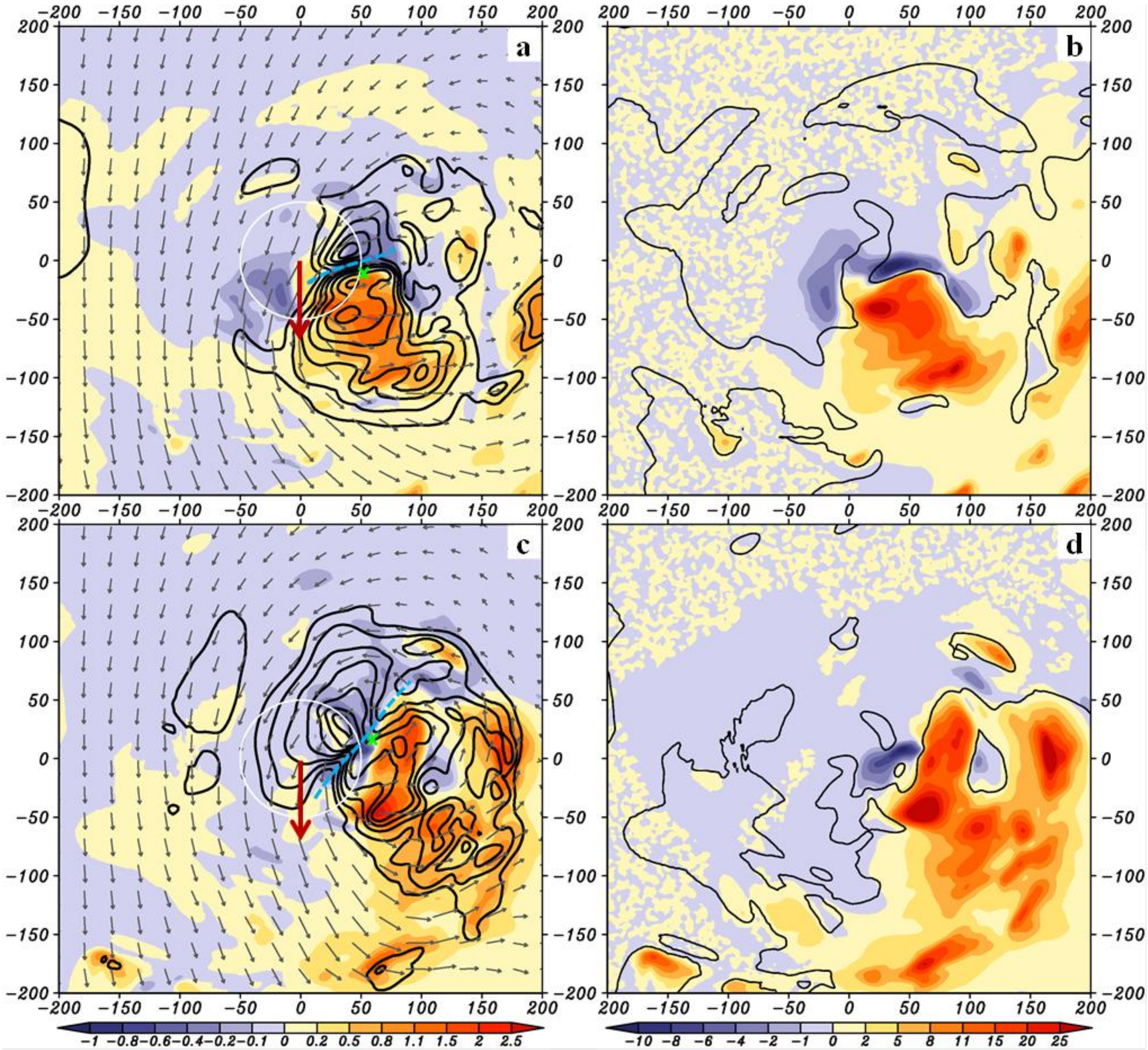

Figure 9: Hourly averaged vertical motion (shading) superposed with potential temperature anomaly (black contours at 0.5 K interval), shear vector (red arrows), and storm-relative flow vector (grey arrows) at 8-km altitude for (a) averaged between 54 – 55 h, corresponding to 0000-0100 UTC 29 Aug; and (c) averaged between 57 – 58 h, corresponding to 0300 – 0400 UTC 29 Aug. The white circle indicates the 50-km radius, and the blue dashed line indicates the cooling that separates diabatic heating from subsidence warming. The green cross indicates the circulation center at 8-km altitude. (b) and (d) show the hourly averaged diabatic heating for 54 – 55 h and 57 – 58 h respectively. The black contours show the zero vertical motion.

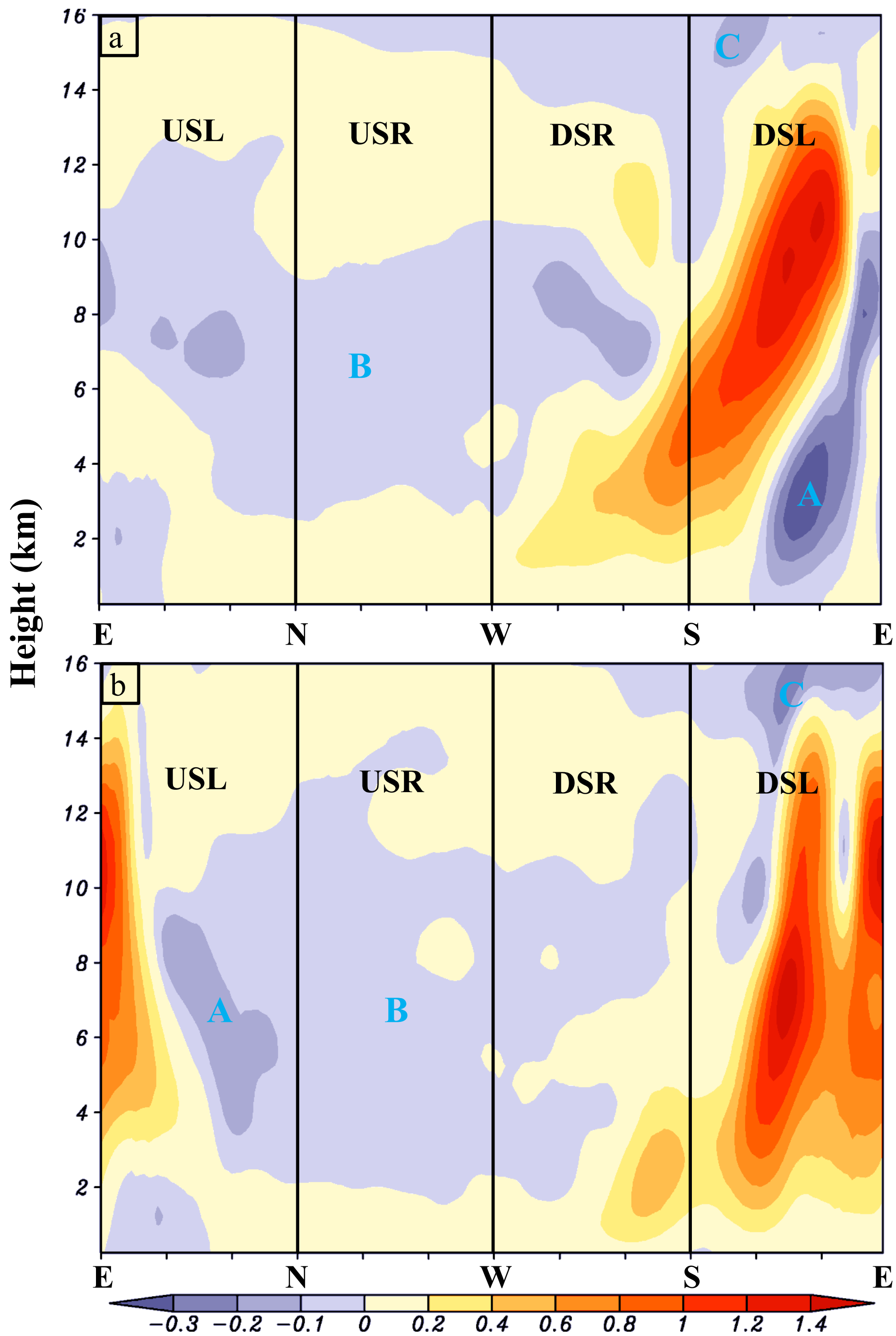

Figure 10: Azimuth-height cross section of ring-averaged (50 km ≤ r ≤ 100 km) vertical motion and time averaged between (a) 54 – 55 h and (b) 57 – 58 h. Blue letter “A”, “B” and “C” indicate convective-scale downward motion, shear-driven mesoscale downward motion and stratospheric detrainment downward motion, respectively.

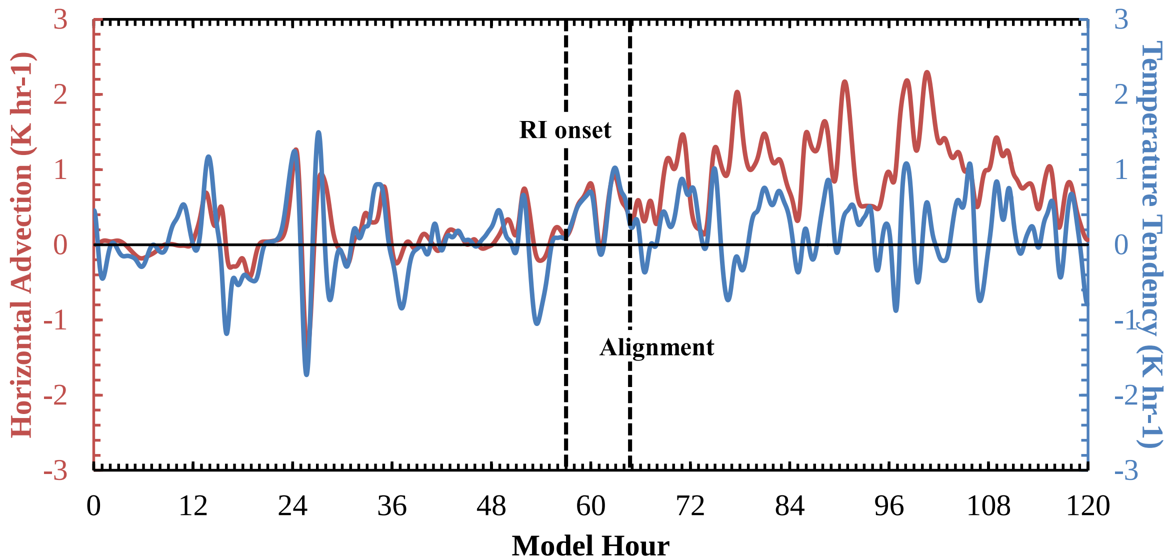

Figure 11: Time series of horizontal advection of potential temperature (red line) and temperature local tendency (blue line) averaged over 8-14 km within a 15-km radius. Black dashed lines indicate the timing of RI onset and vertical alignment.

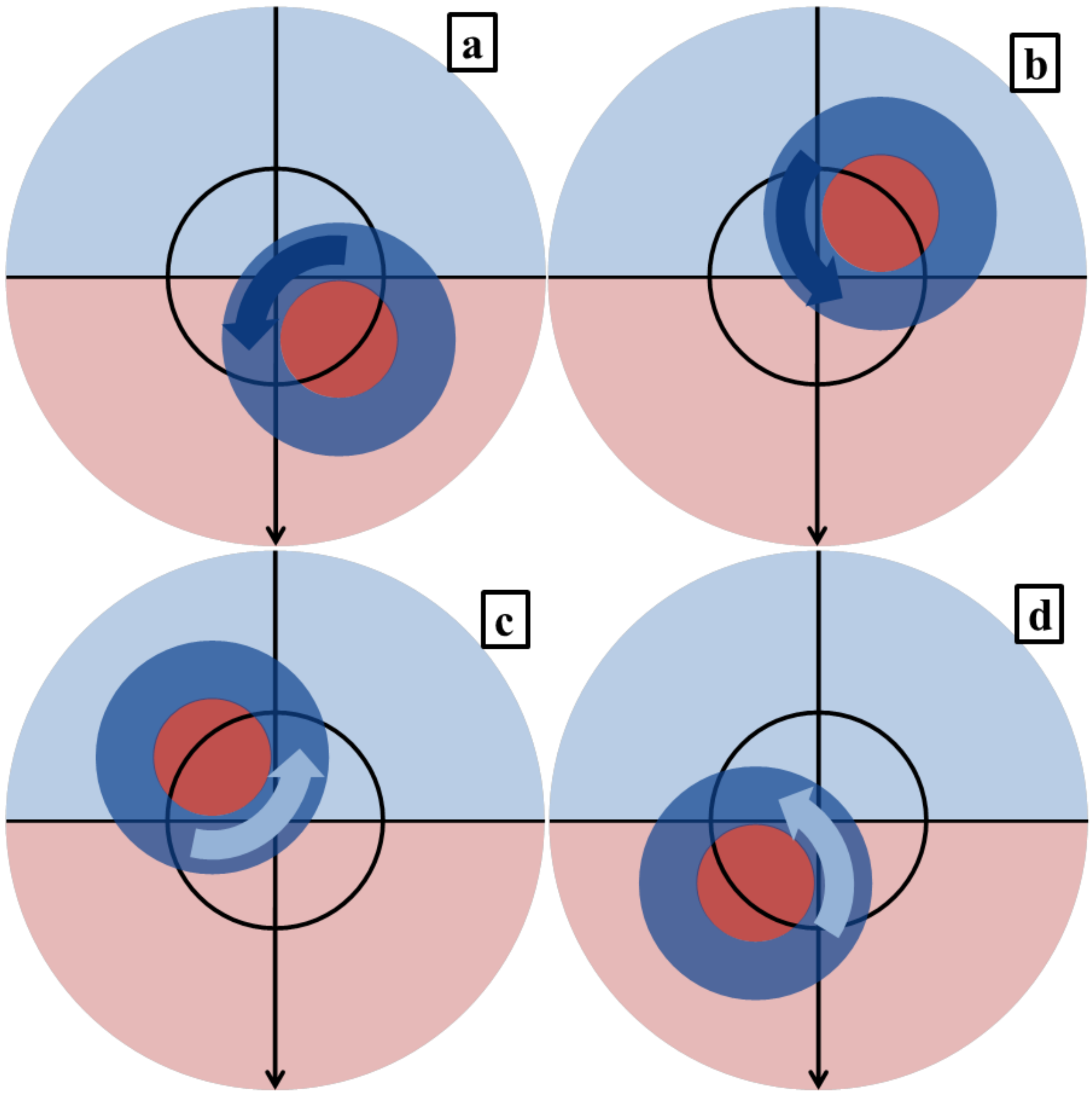

Figure 12: Schematic depiction of configuration of shear-induced mesoscale subsidence (light blue semicircle), mesoscale ascent (light red semicircle), CBs (dark red circle), and convective-scale compensated subsidence (dark blue ring). The black circle indicates the RMW at the surface, and the black arrow shows the shear direction (northerly shear). The thick blue arrow indicates the upper-level flow associated with CBs. For CBs located in (a) downshear-left and (b) upshear-left, convective-scale subsidence is superposed on the mesoscale subsidence. For CBs located in (a) upshear-right and downshear-right, convective-scale subsidence is superposed on the mesoscale ascent.

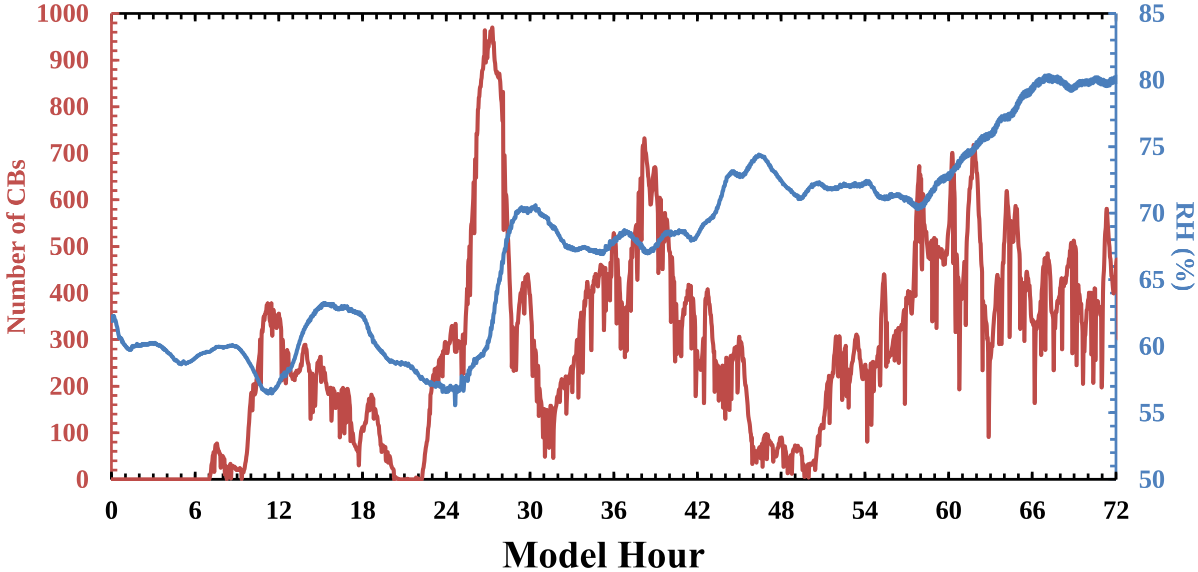

Figure. 13: Time series of the number of CBs and domain averaged relative humidity (400 km × 400 km × 14 km).

Non-Rendered Figure

Click here to download Non-Rendered Figure: Fig1.pdf

Non-Rendered Figure

Click here to download Non-Rendered Figure: Fig3.pdf

Non-Rendered Figure
Click here to download Non-Rendered Figure: Fig4.pdf

Non-Rendered Figure

Click here to download Non-Rendered Figure: Fig5.pdf

Non-Rendered Figure

Click here to download Non-Rendered Figure: Fig7.pdf

Non-Rendered Figure
Click here to download Non-Rendered Figure: Fig9.pdf

Non-Rendered Figure
Click here to download Non-Rendered Figure: Fig10.pdf

Non-Rendered Figure
Click here to download Non-Rendered Figure: Fig13.pdf